J. Fluid Mech. (2006), *vol.* 564, *pp.* 361–393.
doi:10.1017/S0022112006001431 Printed in the United Kingdom

Homogeneous and isotropic turbulence modulation by small heavy ($St \sim 50$) particles

By WONTAE HWANG† AND JOHN K. EATON

Department of Mechanical Engineering, Stanford University, Stanford, CA 94305, USA

(Received 9 March 2005 and in revised form 7 March 2006)

The interaction of a dilute dispersion of small heavy particles with homogeneous and isotropic air turbulence has been investigated. Stationary turbulence (at Taylor micro-scale Reynolds number of 230) with small mean flow was created in a nearly spherical sealed chamber by means of eight synthetic jet actuators. Two-dimensional particle image velocimetry was used to measure global turbulence statistics in the presence of spherical glass particles that had a diameter of 165 μm, which was similar to the Kolmogorov length scale of the flow. Experiments were conducted at two different turbulence levels and particle mass loadings up to 0.3. The particles attenuated the fluid turbulence kinetic energy and viscous dissipation rate with increasing mass loadings. Attenuation levels reached 35–40 % for the kinetic energy (which was significantly greater than previous numerical studies) and 40–50 % for the dissipation rate at the highest mass loadings. The main source of fluid turbulence kinetic energy production in the chamber was the speakers, but the loss of potential energy of the settling particles also resulted in a significant amount of production of extra energy. The sink of fluid energy in the chamber was due to the ordinary viscous dissipation and extra dissipation caused by particles. The extra dissipation was greatly underestimated by conventional models.

1. Introduction

Particle-laden turbulent flows are prevalent in natural and industrial environments. Some examples observed in nature are dust storms, volcanic ash eruptions and avalanches. Industrial applications include chemical reactors, fluidized beds and pollution abatement systems. The addition of particles to a turbulent flow poses a very interesting and challenging problem, where not only are the particles dispersed by the turbulence, but the turbulence itself might also be modulated. Depending on the particle and flow characteristics, the turbulence levels of the carrier phase can be attenuated or augmented. Even with negligible volume fractions of particles, attenuation levels of up to 80 % have been observed in the experiments of Kulick, Fessler & Eaton (1994) and Paris & Eaton (2001). Turbulence modulation can thus greatly affect the performance of industrial applications if not properly considered. The underlying physics of this phenomenon, however, are still not well understood. There is a need for experiments in simple flows to increase the understanding of this phenomenon and to create a database for model developers.

† Present address: Engine Combustion Department, Combustion Research Facility, Sandia National Laboratories, PO Box 969, MS 9053, Livermore, CA 94551, USA.

1.1. *Previous work*

Over the years, many workers have studied the phenomenon of turbulence modulation by particles. Since industrial particle-laden turbulent flows are complex by nature, much of the work has focused on simple free-shear, wall-bounded or homogeneous flows.

Wall-bounded turbulence experiments have relevance to the present study, especially those in pipes and channels. Pipe flows have been studied extensively because of their widespread use in industry for pneumatic conveying of powder. The initial focus was mostly on the modification of pressure drop owing to particles. However, a satisfactory prediction of the pressure drop could not be made without information on the particle–fluid interactions. The experimental results of Carlson & Peskin (1975), Maeda, Hishida & Furutani (1980), Lee & Durst (1982), Tsuji & Morikawa (1982) and Tsuji, Morikawa & Shiomi (1984) indicated that turbulence intensities increased owing to large particles and decreased owing to small particles, with modification generally increasing with particle loading. Fully developed channel flows have been examined widely owing to their attractive properties (Paris & Eaton 2001). There is no decay of turbulence kinetic energy in the streamwise direction like grid-generated turbulent flows. Mechanisms for kinetic energy production, transport and dissipation all occur across the channel. At the centreplane, there is no production owing to symmetry, and the turbulence is approximately homogeneous and isotropic. Kulick *et al.* (1994), Paris & Eaton (2001) and Kussin & Sommerfeld (2002) investigated air channels and showed that the turbulence was attenuated with increasing particle Stokes numbers, mass loadings and particle Reynolds numbers of small particles. The power spectra indicated that energy was extracted at large scales and augmented at small scales. Sato & Hishida (1996), Sato *et al.* (2000), Suzuki, Ikenoya & Kasagi (2000) and Kiger & Pan (2002) examined water channels and observed turbulence augmentation. Experiments have also been conducted in boundary layers (e.g. see Rogers & Eaton 1991) and sudden expansions (e.g. see Hishida & Maeda 1991; Hardalupas, Taylor & Whitelaw 1992; Fessler & Eaton 1999).

The current study addresses homogeneous and isotropic turbulence, which is the most basic type of turbulence. This type of flow enables the study of fundamental particle–fluid interactions, but it has been difficult to create in the laboratory. Stationary homogeneous turbulence self-induced by settling particles was investigated by Parthasarathy & Faeth (1990), Mizukami, Parthasarathy & Faeth (1992) and Chen, Wu & Faeth (2000) using laser-Doppler velocimetry (LDV) in stagnant water, stagnant air and a counterflowing upward wind tunnel, respectively. The dissipation rate, ϵ, was calculated from the loss in potential energy of the particles. The carrier-phase velocity fluctuations were only a function of ϵ and particle drag properties. Grid-generated turbulence has also been examined, as production and transport of turbulence kinetic energy can be neglected in the absence of mean shear. Schreck & Kleis (1993) examined a downward wind tunnel using LDV and observed a monotonic decrease in turbulence intensities with increasing loading. Geiss *et al.* (2004) investigated a downward water tunnel with phase-Doppler anemometry (PDA) and did not notice any changes in the turbulence kinetic energy decay rate for small particles, but observed a decreased decay rate for larger particles at a heavier loading. Nishino & Matsushita (2004) used an upward water flow to create a quasi-stationary suspension of particles, which eliminated the complex transfer of potential to kinetic energy of settling particles. They observed augmentation of the turbulence. Yang & Shy (2005) first demonstrated experimental results of modification of homogeneous and isotropic air turbulence created by counter-rotating fans in a cruciform vessel, owing to small

solid particles with time constants of the order of the Kolmogorov time scale and particle Reynolds numbers less than unity.

Since it has been difficult to create homogeneous and isotropic turbulent flow in the laboratory, many workers have attempted to use numerical simulations as a means of examining this type of flow. Direct numerical simulations (DNS) with a point-force momentum coupling algorithm to account for the particles have been used by Squires & Eaton (1990) and Boivin, Simonin & Squires (1998) to examine stationary homogeneous and isotropic turbulence. The simulations showed that with increasing mass loadings, the turbulence kinetic energy and dissipation rate decreased, while the energy spectra increased at high wavenumbers relative to low wavenumbers. Decaying homogeneous and isotropic turbulence was examined by Elghobashi & Truesdell (1993), Druzhinin & Elghobashi (1999), Sundaram & Collins (1999), Druzhinin (2001) and Ferrante & Elghobashi (2003). Decay rates and spectra of the fluid kinetic energy and ϵ changed depending on the particle size, inertia, loading, and the existence of gravity. Maxey *et al.* (1997) used Gaussian envelopes centred on the particles to represent the particle force fields, and examined forced and decaying turbulence laden with settling particles. They noticed that the turbulence had an axisymmetric instead of an isotropic structure. Burton & Eaton (2003) conducted 'true' DNS of decaying homogeneous and isotropic turbulence by fully resolving the flow around a single particle and observed that the fluid kinetic energy and ϵ was modulated only in the vicinity of particles. Since DNS is still computationally expensive, Boivin, Simonin & Squires (2000) used large-eddy simulations (LES) with a dynamic mixed model to examine the fluid–particle energy exchange in stationary homogeneous and isotropic turbulence.

There have been efforts to classify the numerous different experimental results and identify the important parameters that control turbulence modulation. Gore & Crowe (1989) compiled data from many turbulent gas and liquid flows with a dispersed phase (i.e. particles, droplets or bubbles) at the centreline of pipes and jets, and concluded that particles smaller than a characteristic length of the energetic eddy attenuated the turbulence whereas larger particles augmented it. Hetsroni (1989) also reviewed various jet and pipe flow experiments and suggested that particles with low particle Reynolds number, Re_p, suppressed the turbulence whereas particles with $Re_p > 400$ enhanced it owing to vortex shedding. These parameters could not indicate how much the turbulence would be modified. Eaton (1994) reviewed studies of homogeneous and wall-bounded flows, and found that turbulence attenuation was affected by the particle Stokes number, St, mass loading ratio, ϕ, and changes in flow structure caused by preferential concentration of particles, in addition to the particle diameter, d_p, and Reynolds number, Re_p. A map of turbulence modification regimes that was a function of particle Stokes number and volume fraction, α_p, was presented by Elghobashi (1994). In addition to these parameters, the flow Reynolds number, Re, and density ratio between particle and fluid, ρ_p/ρ_f, might also be important. Evidently, there is still no consensus on what causes turbulence modulation and when it occurs.

1.2. *Objectives*

There needs to be a better physical understanding of particle–turbulence interaction in order to be able to predict turbulence modulation. The objective of this study was to add to the knowledge base by experimentally investigating the ideal case of a uniformly dispersed array of heavy particles (without preferential concentration) interacting with stationary homogeneous and isotropic air turbulence in the absence

of mean flow (fluid velocity, $\boldsymbol{u} = \boldsymbol{u}'$). The experiments were conducted with particles falling through the turbulence at a certain settling velocity (particle velocity, $\boldsymbol{v} = \boldsymbol{v}_t + \boldsymbol{v}'$). The following specific conditions were considered. The particulate phase was spherical monodisperse glass beads, with a small but finite diameter, $d_p \sim \eta_k$ (Kolmogorov length scale). The particle Reynolds number based on the particle diameter, $Re_p \sim 10$, so the particle wake distortions extend several particles downstream and cannot be neglected (Eaton, Paris & Burton 1999). The particles were relatively heavy, with $\rho_p/\rho_f \sim 2000$ and particle Stokes number based on the Kolmogorov time scale, $St_k \sim 50$. The flow was dilute yet appreciably laden with particles, with maximum $\alpha_p \sim 10^{-4}$, $\phi \sim 0.3$, and total number of particles, $N_p \sim 5 \times 10^6$, which corresponded to an inter-particle spacing of $l_p \sim 15 d_p$. These conditions are representative of those found in many industrial applications and natural environments.

In this study we aim to provide global turbulence statistics of the flow. We did not directly attempt to temporally or spatially resolve the nonlinear and unsteady particle–turbulence interactions and resulting flow distortion near the particle surface. Instead, ensemble averages of instantaneous realizations of the flow field taken at a sampling rate of 2 Hz (to obtain independent samples) are reported. It is important to note that this flow is statistically stationary even with the addition of particles. Ensemble-averaged statistics conditioned on phase are representative of modifications of the overall turbulence.

The experimental facility and measurement techniques are described in § 2. Results of carrier-phase turbulence modulation are presented and discussed in § 3. A summary of the work may be found in § 4.

2. Experimental facility and techniques

The experiments were conducted in a chamber capable of creating homogeneous and isotropic air turbulence with no mean flow. A description of the flow facility and single-phase (unladen) flow qualification results of stationary and decaying turbulence have been presented by Hwang & Eaton (2004*a*). This study examined stationary turbulence at two different energy levels. Particles fell through a long chute and entered the chamber at their terminal velocity. A detailed description of the entire experimental set-up can be found in Hwang & Eaton (2004*b*).

2.1. *Experimental set-up and procedures*

The turbulence chamber is a symmetric Plexiglas box with one side being 410 mm. The corners were cut off to make it approximately internally spherical. The turbulence was generated by synthetic jet actuators which were mounted on the eight corners. The actuators used 165 mm polypropylene cone woofers (60 W r.m.s., uniform frequency response between 55 Hz and 3 kHz), made by Pioneer (model number C16EU20-51D), which made them robust and optimal for particle-laden flow studies. Random frequency (between 90 and 110 Hz) and phase sine waves were individually amplified by a Phast PLB-Amp8 power amplifier and sent to the speakers. The synthetic jets passed through ejector tubes which increased the flow and decreased the velocity of the jet. Wire mesh was attached to the end of the ejector tubes as turbulence grids to introduce intermediate scales into the jet.

The particle feeding system is shown in figure 1(*a*). Particles were fed from an Accurate Model 302 volumetric screw feeder which was located on the roof of the laboratory, 3.1 m above the top of the chamber. The screw feeder gave a constant

FIGURE 1. (*a*) Particle feeding system. From top to bottom: screw feeder, particle-dispersing sieves, and particle chute (going through the ceiling). (*b*) Experimental setup. Counterclockwise from top: particle chute, turbulence chamber, Kodak ES1.0/10 camera, Continuum Minilite PIV Nd:YAG laser, and sheet-creating optics.

outflux of particles, with negligible high-frequency and low-frequency temporal fluctuations. An 18-mesh (0.432 mm diameter wire with 1.00 mm opening) copper screen was installed around the exit of the discharge cylinder to reduce spatial unsteadiness as the screw turned. The particles fell through a PVC funnel, which

reduced the spatial non-uniformity even further. The funnel guided the particles to the centre of the chute, and they were dispersed by five equally spaced standard sieves which had mesh sizes of 30 (0.390 mm diameter wire with 0.600 mm opening), 30, 35 (0.340 mm diameter wire with 0.500 mm opening), 35 and 40 (0.290 mm diameter wire with 0.425 mm opening), from top to bottom. A honeycomb followed to reduce horizontal motion caused by the screens. The particles then fell through a 152 mm diameter, 2.5 m long chute which reached from the roof down through the ceiling to the top of the chamber. The chute was long enough for the particles to reach their terminal velocity before entering the chamber. A 155 mm diameter hole was made in the top of the chamber, and a flange was placed on top of it. A rectangular rubber gasket rolled into a cylinder was glued together and connected to the chute and flange to ensure that the chute was isolated from the chamber vibrations. The particles settled and piled up at the bottom of the chamber in a symmetric pattern with a small peak in the centre. This suggested that the particle feeding system was performing well, and that the overall particle loading was fairly uniform even as it dropped through the turbulence. The peak at the centre was caused by the particles dropping from the screw feeder into the centre of the chute before reaching the sieves which dispersed them. The experimental set-up is depicted in figure 1(*b*).

The flow seeding system was similar to that described by Hasselbrink & Mungal (2001). A fluidized bed seeder was used in conjunction with a cyclone separator to seed the flow with small flow tracers. Deagglomerated alumina particles 0.3 μm in size from Praxair Surface Technologies were used as the tracers. Seeded air entered the turbulence chamber through a port which pointed to the centre of the chamber. The port was located on one of the chamber sidewalls beneath the optical glass window for the camera. The air was filtered with a high-efficiency inert air filter before exiting the chamber. Well before data acquisition was initiated, the chamber was fully seeded and the seeding air flow turned off.

Overheating of the speakers in the synthetic jet actuators caused the turbulence statistics to be somewhat inconsistent. To keep the turbulence levels constant, air jets (at 55 p.s.i.g.) from a 1.6 mm nozzle were blown on the speaker magnets to cool the speakers. After about 45 min, the speakers reached a thermally stable state and the variation in the turbulence statistics became small. The speaker magnet temperature rise was limited to 10 °C (as compared to 30° without cooling), and the synthetic jet velocity decrease was limited to 10 % (as compared to 20 % without cooling). Thus, the speakers were operated with the cooling jets on for about 45 min before the experiments started. This alleviated most of the problems regarding speaker overheating. However, for the sake of comparison and also to normalize results, a set of unladen flow measurements was taken before each set of particle-laden flow measurements. After finishing taking the particle-laden flow data set, the screw feeder was turned off and the flow was allowed to recover for a few minutes. Then a second unladen flow data set was acquired to determine how the unladen flow recovered. All three sets of measurements (pre-unladen, laden and post-unladen) were sequentially acquired with the speakers running continuously. Each data set consisted of 20 runs of 50 image pairs each, totalling 1000 image pairs.

2.2. *Particle characteristics and mass loading calibration*

The glass particles were obtained from USF Surface Preparation and size sorted by Vortec Products Company. Coulter counter measurements indicated that the mean particle diameter, d_p, was 165 μm, with a standard deviation of 15.7 μm. The density of the particles, ρ_p, was given as 2500 kg m^{-3}. The Stokes particle time constant is

given as

$$\tau_{p,s} = \frac{\rho_p d_p^2}{18\mu}, \tag{2.1}$$

where μ is the fluid kinematic viscosity. The modified particle time constant is given as (Fessler & Eaton 1999)

$$\tau_p = \frac{\tau_{p,s}}{1 + 0.15 Re_p^{0.687}}, \tag{2.2}$$

where Re_p is defined using the particle slip velocity, which can be calculated when the nonlinear drag force equals the gravitational force. The Stokes time constant was calculated to be 210 ms, and the modified time constant was 114 ms. The particle Stokes number based on the modified time constant and Kolmogorov time scale of the unladen flow is defined as

$$St_k = \frac{\tau_p}{\tau_k}, \tag{2.3}$$

and had values of 59 and 48 for the higher-energy (twice the turbulence kinetic energy $q^2_{\phi=0} = 1.44\,\mathrm{m^2\,s^{-2}}$) and lower-energy ($q^2_{\phi=0} = 1.12\,\mathrm{m^2\,s^{-2}}$) cases, respectively. Wood, Hwang & Eaton (2005) used the same apparatus at the same operating conditions to show that $St_k = 8.1$ glass particles did not display preferential concentration. We can therefore conclude that the much larger St_k particles used in this study were not in the range where preferential concentration is observed.

The settling velocity of the 165 μm glass beads in still air was measured at the centre of the chamber using particle tracking velocimetry (PTV) to see if the particles had reached their terminal velocity. The average settling velocity of the glass beads was found to be $1.20\ \mathrm{m\,s^{-1}}$. The images were divided into two horizontal bands to see if the particles were accelerating within the images. The mean settling velocities for both bands were the same as the overall mean settling velocity within measurement uncertainty. Therefore, it was concluded that the particles had reached their terminal velocity of $v_t = 1.20\,\mathrm{m\,s^{-1}}$. This was slightly larger than the terminal velocity calculated from the modified time constant as $v_t = \tau_p g = 1.12\,\mathrm{m\,s^{-1}}$.

The particle mass loading ratio, ϕ, has been conventionally defined as the ratio of mass fluxes between particles and air ($\dot{m}_p/\dot{m}_a$). This is suitable for wind tunnels, but we had to use a slightly different definition since there is no steady flow of air in the chamber. Here the particle mass loading was defined as the ratio of the mass of dispersed particles to the mass of air in the chamber (which was considered constant). The mass of the dispersed particles could not easily be calculated or measured since the particles did not fall exactly at their terminal velocity within the chamber owing to the downward and upward motion of the turbulent eddies. The number of particles dispersed reached an equilibrium state, as the mass of particles entering the chamber and settling at the bottom reached a steady rate. The weak secondary flow in the chamber was not strong enough to lift the heavy glass particles that had settled on the bottom.

A calibration scheme was devised to obtain the mass loading from the number of particles in the images. It consisted of three steps, without the synthetic jet actuators operating. First, the particles were dropped down the chute, and the particle mass flux, $\dot{m}_p$, was obtained at five different screw feeder settings by measuring the accumulating mass of particles on a plate at the bottom of the chamber using a load cell. The mass increased very linearly with time, and the slope of each line corresponded to the mass flux of particles. The second step was to calculate ϕ using the mass of air, M_a, in a cylindrical control volume having a diameter equal to that of the particle chute,

and height, H, the same as that of the chamber, and the mass of dispersed particles, M_p $(=\dot{m}_p H/v_t)$, settling within this imaginary cylinder. The mass loading ratio of the control volume could then be calculated as $\phi = M_p/M_a$. The final step involved taking images of the settling particles and obtaining the average number of particles per image for each screw feeder setting and corresponding ϕ. The mass loading ratio, ϕ, could thus be written as a function of the number of particles in the images, n_p:

$$\phi = 4.92 \times 10^{-4} n_p + 0.00275. \tag{2.4}$$

For the actual experiments where the synthetic jet actuators were running and the particles were dispersed by the turbulence, ϕ could thus be obtained from (2.4) by counting the number of particles per image. There were no additional uncertainties involved when using (2.4) to obtain ϕ with the turbulence turned on, aside from the inherent uncertainties involved with counting the number of particles from the images.

2.3. *Measurement system and techniques*

Two-dimensional particle image velocimetry (PIV) measurements were obtained at the centre of the chamber in a $40 \times 40\,\mathrm{mm}^2$ region. A Continuum Minilite PIV dual-head Nd:YAG laser (25 mJ/pulse at 532 nm) was used with sheet-creating optics to illuminate the imaging domain. The waist of the light sheet was at the centre of the imaging domain, and the thickness was approximately 0.4–0.5 mm throughout the imaging domain. A Kodak ES1.0/10 10 bit CCD (1018×1008 resolution) camera was used in conjunction with a 55 mm micro-Nikkor lens at f/2.8. The camera was operated in double-triggered mode with an image pair time separation of around 100 μs, which was small enough compared to the Kolmogorov time scale of approximately 2 to 3 ms to resolve the small scales of turbulence temporally. The lasers and camera were triggered by LabVIEW at 2 Hz to obtain independent samples of the flow. It should be noted that the main purpose of the study was to report overall statistics, not to describe the temporal evolution of the turbulence. Image acquisition was achieved with an EPIX PIXCI-D frame grabber board and 450 MHz Pentium II desktop computer.

The PIV algorithm was written in Matlab by Han (2001) and incorporated recursive interrogation window offset and reduction to increase the spatial resolution and accuracy of the measurements. The final iteration used a window size of 32×32 pixels at 50 % overlap, resulting in a velocity vector field of 59×59 vectors. Spurious vectors that remained after the final iteration of the PIV algorithm were not used in computing the statistics. Sub-pixel accuracy was obtained through a Gaussian estimator. Displacement uncertainty was larger than the ± 0.1 pixels originally proposed by Willert & Gharib (1991), and was estimated at approximately ± 0.2 pixels due to particles. The images were processed with a 2.2 GHz Intel Xeon dual-processor workstation at 30 s per image pair.

The displacements were biased toward integer values because the tracer particles appeared small in the images. This 'peak-locking' effect was manifested as peaks in the displacement probability density functions (PDF). A technique that involved equalizing the histogram of the sub-pixel displacements (Roth & Katz 2001) was used to eliminate the peak-locking. The displacements resulted in a change of only 0.01 pixels per vector on average, and therefore the turbulence statistics were not affected with peak-locking removal. This inherently suggests that the peak-locking did not adversely affect the original measurement accuracy that much. The measurement

uncertainty was reduced slightly from the peak-locking elimination, by approximately 5 %.

The dispersed phase had to be eliminated from the images to obtain accurate continuous-phase PIV measurements from the flow tracers. Figure 2 shows a sample $40 \times 40\,\mathrm{mm}^2$ PIV negative image of the 0.3 μm alumina flow tracers and large 165 μm glass particles at $\phi = 0.23$. The camera was intentionally slightly defocused to make the tracers appear larger to reduce peaklocking effects. Defocusing can cause Mie scattering interference patterns for the tracer particle images, which would modulate the PIV cross-correlation function and cause errors in determining the particle displacement. However, the defocused tracer particle images were typically only 2–3 pixels in diameter, so the interferograms could not be observed with the current camera resolution, and was thus deemed to have only a very minor effect on displacement calculation. Defocusing unfortunately made it difficult to discriminate some of the agglomerated tracers from the glass particles in the images. Also, some of the glass particles appeared very bright and large (whereas they should theoretically have been only about 5 pixels) because they fully saturated the CCD, as can be seen from some of the particles on the right-hand side of figure 2. This imaging artefact made the concentration appear more non-uniform (as if particles were colliding) than it actually was. It should be noted that the volume fraction of particles was of the order of 10^{-4}, so particle collision effects were minimal. The background noise levels also varied throughout the image owing to local scattering of light from these bright particles. Some particles were on the outer edge of the laser sheet and appeared large and dim because they were out of focus and did not scatter enough light.

A spatial median filtering technique proposed by Kiger & Pan (2000) was used to separate the two phases. Median filtering is effective at removing noise which consists of strong spikelike components (e.g. tracers), while preserving sharp edges of objects (e.g. large particles) (Gonzalez & Woods 1993; Bracewell 1995). Applying a 3×3 filter window to the sample image of figure 2 results in the image of large particles in figure 3(*a*). Subtracting this image from the original image gives the image of tracers in figure 3(*b*). The separated image of the large particles included the oversized tracer agglomerates, and thus the resulting image of tracers did not contain any large glass particles or tracer agglomerates. Gas-phase statistics could therefore be measured using PIV. The technique was validated by comparing results from a single-phase tracer image pair and a median-filter separated tracer image pair obtained from a composite two-phase image pair (see Hwang & Eaton 2004*b*), where images of glass particles only were added on to the single-phase tracer image pair. The velocity maps and statistics were almost the same, with differences of 3 % in the mean velocities and 1 % in the root mean square (r.m.s.) velocities. We concluded that the gas-phase results from the median-filtered images were not significantly affected by remnant particle images, i.e. particle cross-talk was small.

2.4. *Experimental uncertainty*

The particle-laden flow experiments were conducted at three mass loadings for both the higher-energy ($q^2_{\phi=0} = 1.44\,\mathrm{m}^2\,\mathrm{s}^{-2}$) and lower-energy ($q^2_{\phi=0} = 1.12\,\mathrm{m}^2\,\mathrm{s}^{-2}$) cases. The uncertainties in ϕ were estimated from the calibration method outlined in § 2.2 (see Hwang & Eaton 2004*b*). The mass loadings and their estimated uncertainties (at 95 % confidence levels) for the higher-energy case were 0.015 ± 0.0029, 0.10 ± 0.0097, and 0.23 ± 0.017. For the lower-energy case they were 0.015 ± 0.0029, 0.099 ± 0.0090 and 0.29 ± 0.018.

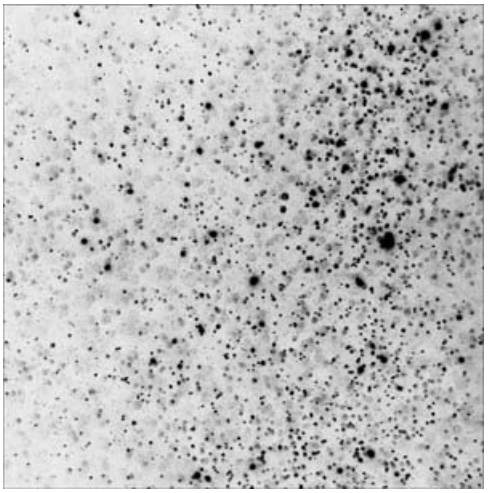

FIGURE 2. Sample negative image of 165 μm glass particles and 0.3 μm alumina flow tracers.

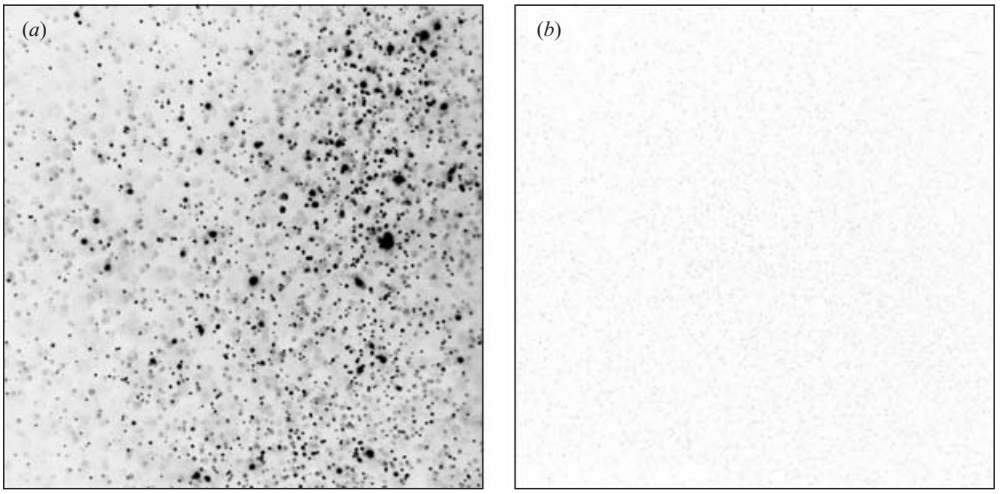

FIGURE 3. Separated image of (*a*) 165 μm glass particles and (*b*) 0.3 μm alumina flow tracers.

Although the velocity uncertainty was about 0.1 m s^{-1} for a PIV time separation of 100 μs, the mean flow measurements were repeatable to within about $\pm$0.0015 m s^{-1}, which corresponded to approximately 1 % of the mean flow, at 95 % confidence. This uncertainty was much smaller than that reported in Hwang & Eaton (2004*a*), probably because the speakers were actively cooled and the data were taken after the speakers had thermally stabilized. The room temperature was also held fairly constant and did not play a role. The uncertainty remained small even as particles piled up on the bottom of the chamber. Error bars for the mean flow were thus very small and not shown on the figures to avoid confusion.

The uncertainties for the r.m.s. velocity and turbulence kinetic energy were estimated at approximately 5 % and 6 %, respectively. The uncertainty considered PIV measurement uncertainty, ensemble statistical errors, oversampling due to the 50 % interrogation window overlap, uncertainty due to particles, and uncertainty due to statistics not fully recovering to the unladen state after the particles had stopped

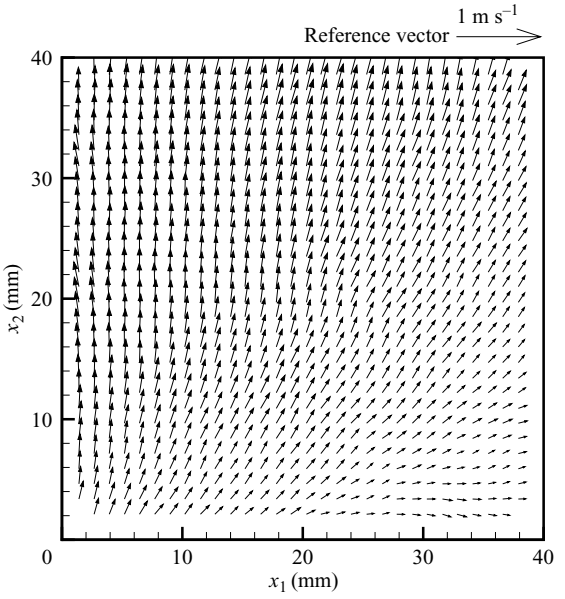

FIGURE 4. Mean fluid velocity field of the pre-unladen flow. Three-quarters of the vectors have been removed for clarity.

falling. The dissipation rate had the abovementioned uncertainties and additional uncertainties involved with calculating velocity gradients and estimating out-of-plane velocity gradients. Although the uncertainty for ϵ was approximated at about 13 %, it was probably larger considering that ϵ was measured from the resolved velocities using a dynamic-equilibrium assumption (see the next section on how ϵ was measured). The out-of-plane motion was minimized by choosing a PIV time separation that was very small, an order of magnitude smaller than the Kolmogorov time scale.

2.5. *Base unladen flow qualification*

Single-phase flow qualification of the turbulence chamber was previously documented by Hwang & Eaton (2004*a*). We report some basic flow qualification results here again because the chamber geometry had been modified with the adddition of the particle chute at the top. Results are from the higher energy pre-unladen case corresponding to the highest ϕ, case B3i (see table 1 in § 3.1). Since the flow was homogeneous, as will be shown in this section, results are presented as spatial and ensemble averages of all the local statistics from each measurement point in the 1000 PIV image pairs. In essence, each PIV interrogation window was considered a separate measurement probe.

There was a small mean flow directed upwards in the measurement region, as can be seen in figure 4. The horizontal mean flow was negligible at 0.063 m s^{-1}, but the vertical mean flow was a bit higher at 0.20 m s^{-1}. This was still less than 30 % of the r.m.s. velocities, which were 0.70 and 0.69 m s^{-1} for the horizontal and vertical directions, respectively. The horizontal and vertical fluctuating velocity PDFs shown in figure 5 both followed a Gaussian distribution. The similarity in r.m.s. velocities was an indication that the flow was isotropic. The spatial average of q^2 was approximately 1.44 m^2 s^{-2}, assuming that the out-of-plane r.m.s. velocity was similar to the in-plane

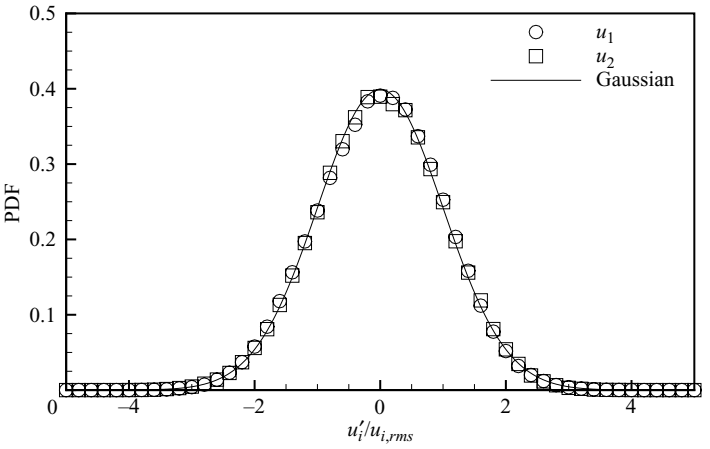

FIGURE 5. Fluctuating fluid velocity PDFs of the pre-unladen flow.

r.m.s. velocities:

$$q^2 \equiv u_{i,rms}u_{i,rms} \cong 3\frac{u_{1,rms}^2 + u_{2,rms}^2}{2}. \tag{2.5}$$

Accurate measurement of the viscous dissipation is very difficult, even in isotropic flows (Raffel, Willert & Kompenhans 1998). We chose to use the LES analogy technique described by Sheng, Meng & Fox (2000). It assumes that the sub-integral scales are in dynamic equilibrium, whereby the sub-grid scale (SGS) energy flux from the integral scale through the inertial sub-range to the Kolmogorov scale is equal to the dissipation rate. Thus, resolved velocity gradients within the inertial sub-range can be used to estimate the turbulence kinetic energy flux, and the dissipation rate can be written as

$$\epsilon \approx \epsilon_{SGS} = -2\tau_{SGS_{ij}}S_{ij}, \tag{2.6}$$

where S_{ij} is the resolved-scale strain rate tensor defined by

$$S_{ij} = \frac{1}{2}\left(\frac{\partial u_j}{\partial x_i} + \frac{\partial u_i}{\partial x_j}\right), \tag{2.7}$$

and $\tau_{SGS_{ij}}$ is the SGS stress tensor, estimated from the Smagorinsky model:

$$\tau_{SGS_{ij}} = -C_s^2\Delta^2|\sqrt{2S_{ij}S_{ij}}|S_{ij}, \tag{2.8}$$

where $C_s = 0.17$ is the Smagorinsky constant and $\Delta = 0.63$ mm is the spatial resolution of the velocity vectors. The spatially averaged dissipation rate was measured to be approximately $4.3\,\mathrm{m^2\,s^{-3}}$. The Taylor microscale and associated Reynolds number are

$$\lambda = \left(\frac{5\nu q^2}{\epsilon}\right)^{1/2}, \quad Re_\lambda = \frac{\lambda(q^2/3)^{1/2}}{\nu}, \tag{2.9a, b}$$

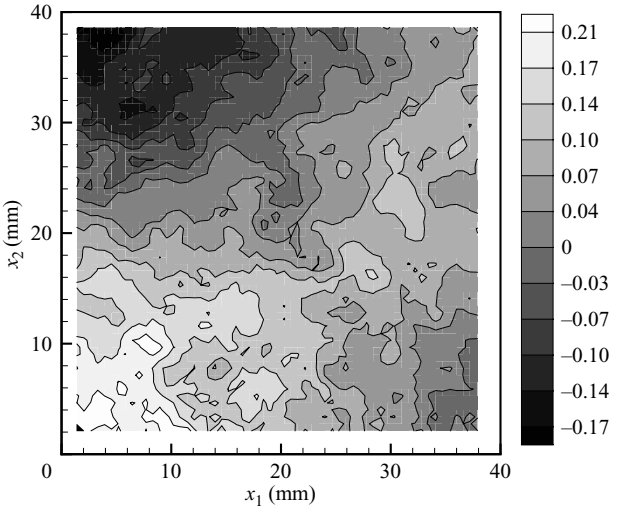

FIGURE 6. Shear-stress correlation coefficient map for the pre-unladen flow.

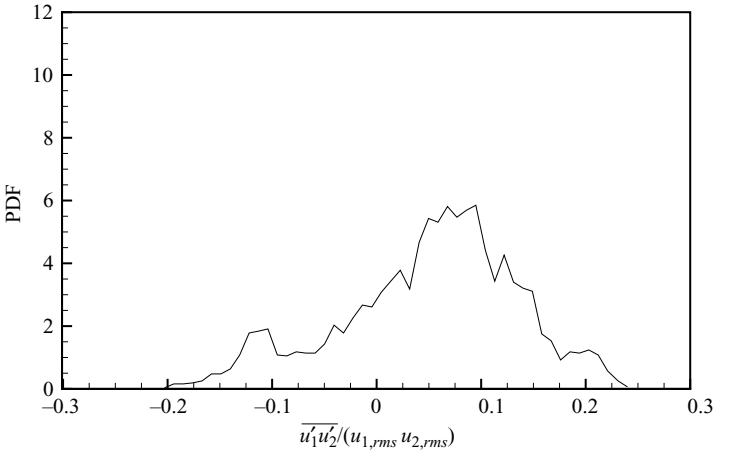

FIGURE 7. Shear-stress correlation coefficient PDF for the pre-unladen flow.

and had spatially averaged values of 5.0 mm and 230, respectively. The Kolmogorov time and length scales are defined as

$$\tau_k = \left(\frac{\nu}{\epsilon}\right)^{1/2}, \quad \eta_k = \left(\frac{\nu^3}{\epsilon}\right)^{1/4}, \tag{2.10a, b}$$

and had spatially averaged values of 1.9 ms and 0.17 mm, respectively. The imaging domain was not large enough to measure the integral length scale directly, but it was estimated to be approximately 80 mm from q^2 and ϵ.

The Reynolds shear stress was examined with the spatial map of the shear-stress correlation coefficient, $\overline{u_1'u_2'}/(u_{1,rms}u_{2,rms})$, which is shown in figure 6 for the pre-unladen flow. It displayed both positive and negative values and had a small average value of 0.050, suggesting that the flow was isotropic. However, the PDF in figure 7 showed a small positive bias with a peak near 0.075. This positive bias was probably due to the mean shear caused by the secondary flow, but was significantly smaller than the value

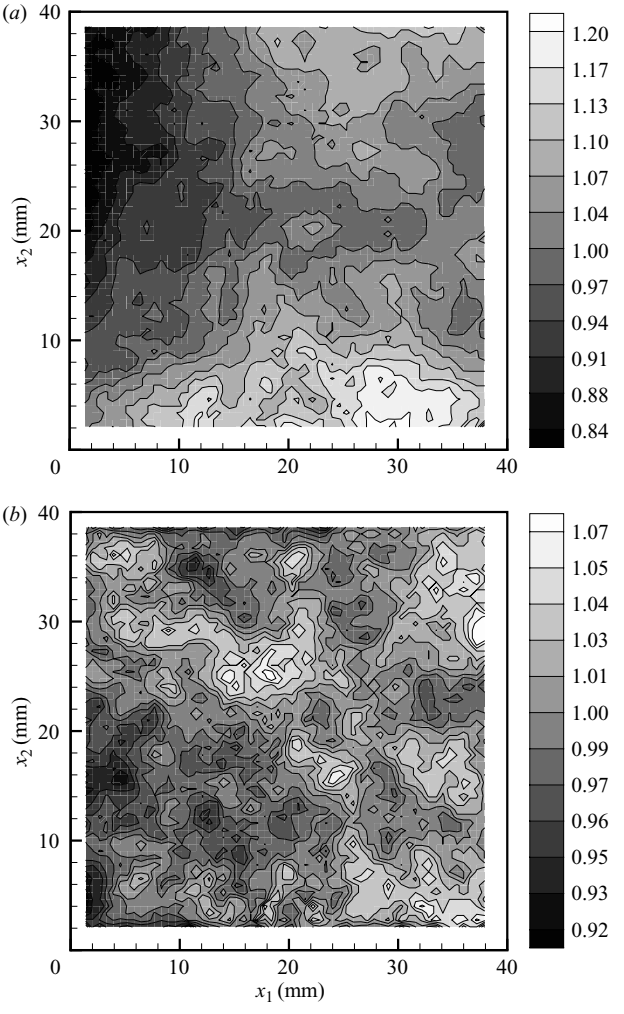

FIGURE 8. Map of (a) isotropy ratio ($u_{1,rms}/u_{2,rms}$) and (b) turbulence kinetic energy normalized by the spatial average ($q^2/\langle q^2 \rangle$) for the pre-unladen flow.

of 0.3–0.4 nominally observed in shear flows. The spatial map of the isotropy ratio, $u_{1,rms}/u_{2,rms}$, is shown in figure 8(a). It had values centred around unity, indicating that the flow was isotropic within the imaging region. The map of q^2 normalized by its spatial average in figure 8(b) also had fairly uniform values near unity, indicating that the flow was homogeneous as well.

The two-point longitudinal velocity correlation coefficient in the horizontal and vertical direction is defined as

$$F_{11}(r) = \frac{\overline{u_1'(x_1, x_2)u_1'(x_1 + r, x_2)}}{u_{1,rms}^2}, \tag{2.11a}$$

$$F_{22}(r) = \frac{\overline{u_2'(x_1, x_2)u_2'(x_1, x_2 + r)}}{u_{2,rms}^2}, \tag{2.11b}$$

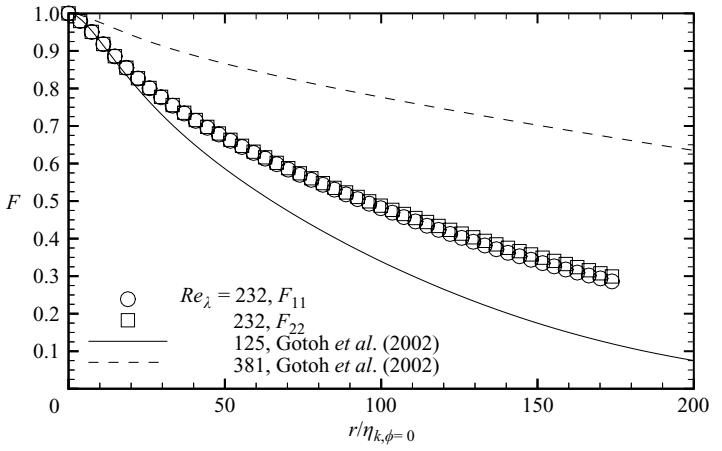

FIGURE 9. Two-point longitudinal velocity correlations for the pre-unladen flow in the horizontal (F_{11}) and vertical (F_{22}) directions.

where r is the separation distance. The correlation coefficients coincided well in both directions (figure 9), again confirming that the flow was isotropic, and were also in between the DNS data of Gotoh, Fukayama & Nakano (2002) at $Re_\lambda = 125$ and 381.

Spatial turbulence kinetic energy spectra can be obtained from two-dimensional PIV data (Liu, Meneveau & Katz 1994; Liu, Katz & Meneveau 1999). The radial energy spectrum function is defined as (Hwang & Eaton 2004*a*)

$$E(k) = \frac{k}{2}\int_0^{2\pi} (\Delta k)^2 \langle \hat{u'}_i(\boldsymbol{k})\hat{u'}_i^*(\boldsymbol{k})\rangle \, \mathrm{d}\theta, \tag{2.12}$$

where k is the wavenumber, Δk is the width of the annulus in wavenumber space with radius $|\boldsymbol{k}| = k$, $\hat{(\cdot)}$ denotes a two-dimensional Fourier transform, and $(\cdot)^*$ denotes the complex conjugate. The procedure for calculating $E(k)$ involved first performing a two-dimensional fast Fourier transform (FFT) of the instantaneous fluctuating velocity field, i.e. the mean velocity field subtracted from each instantaneous velocity field. Then the spatial average (in wavenumber space) of the squared moduli in each annulus was ensemble averaged over all of the image pairs. Radial spectra of the horizontal and vertical velocity components are shown in figure 10 (right-hand scale), along with the universal Kolmogorov spectrum (Liu *et al.* 1999)

$$E_{\alpha\alpha}(k) = 0.535\, C_k \langle\epsilon\rangle^{2/3} k^{-5/3} \qquad \text{(no summation over } \alpha\text{)}, \tag{2.13}$$

where the Kolmogorov constant $C_k = 0.16$, and $\langle\epsilon\rangle = 4.3\,\mathrm{m^2\,s^{-3}}$. One-dimensional longitudinal spectra were obtained along each line of velocity vectors and ensemble averaged over all the image pairs. They are also shown with the Kolomogorov longitudinal spectrum

$$E_{\alpha\alpha}(k_\alpha) = C_k \tfrac{18}{55} \langle\epsilon\rangle^{2/3} k_\alpha^{-5/3}, \tag{2.14}$$

along with DNS data from Yeung & Zhou (1997) at $Re_\lambda = 240$ in figure 10 (left-hand scale). The collapse of the horizontal and vertical components indicated that the flow was isotropic. The smallest wavenumbers corresponding to the integral scales could not be directly measured owing to the limited size of the spatial domain, and the largest wavenumbers corresponding to the dissipative scales could not be directly measured owing to the limited spatial resolution of the measurement system. Within

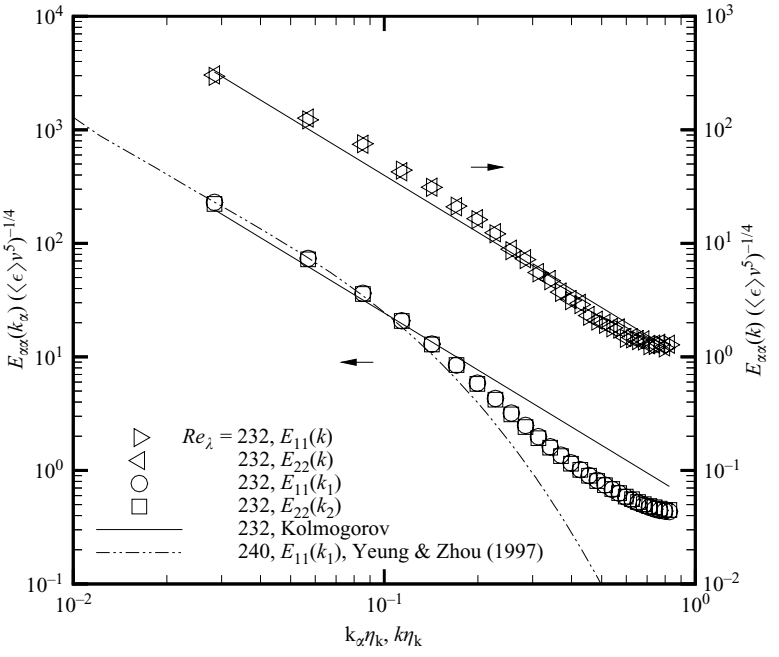

FIGURE 10. Turbulence kinetic energy spectra for the pre-unladen flow. Left: one-dimensional longitudinal spectra. Right: two-dimensional radial spectra.

the limited range of wavenumbers that we could measure, the spectra followed the Kolmogorov $-5/3$ law at the smaller wavenumbers, suggesting that the inertial range was partially being observed. The behaviour of the spectra at the higher wavenumbers was probably due to measurement uncertainty (Liu *et al.* 1994, 1999).

3. Results and discussion

3.1. *Turbulence attenuation*

Each experimental run consisted of three sequential data sets: pre-unladen, laden and post-unladen. Flow statistics were normalized by corresponding results from each pre-unladen data set and ensemble averaged over 1000 PIV image pairs. By plotting the normalized statistics as sequential data points corresponding to pre-unladen, laden and post-unladen data sets, we could see how the flow recovered to its original state. Figure 11 shows an example of this experimental procedure for the horizontal fluctuating velocity. As ϕ is increased, $u_{1,rms}$ is attenuated, and after the particle flow is turned off, it almost recovers to its original pre-unladen value for both turbulence levels. This shows that the particles accumulating at the bottom of the chamber did not affect turbulence levels. For the remainder of this section, normalized flow statistics are presented as functions of particle mass loading for both turbulence levels. The statistics are also spatially and ensemble averaged over the 1000 image pairs, which eliminates the effect of spatial variation of the turbulence attenuation due to any particle loading non-uniformity. The flow statistics are tabulated in tables 1 and 2 for the two turbulence levels.

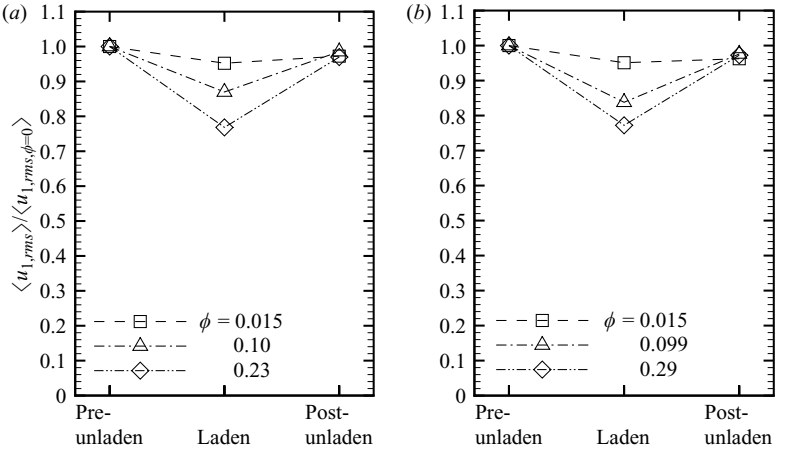

FIGURE 11. Example of experimental procedure. Variation of $u_{1,rms}$ with addition of particles for cases (*a*) $q^2_{\phi=0} = 1.4\,\mathrm{m^2\,s^{-2}}$ and (*b*) $q^2_{\phi=0} = 1.1\,\mathrm{m^2\,s^{-2}}$.

	B1i	G1it	A1i	B2i	G2it	A2i	B3i	G3it	A3i
ϕ	0	0.015	0	0	0.100	0	0	0.231	0
$\langle\overline{u}_1\rangle$ (m s^{-1})	0.0629	0.0578	0.0311	0.0613	0.0635	0.0451	0.0631	0.0898	0.0670
$\langle\overline{u}_2\rangle$ (m s^{-1})	0.174	0.128	0.150	0.206	0.0961	0.149	0.200	0.0045	0.0418
$\langle u_{1,rms}\rangle$ (m s^{-1})	0.689	0.656	0.670	0.683	0.594	0.673	0.695	0.534	0.673
$\langle u_{2,rms}\rangle$ (m s^{-1})	0.676	0.648	0.657	0.668	0.596	0.653	0.687	0.552	0.655
$\langle q^2\rangle$ (m^2 s^{-2})	1.40	1.28	1.32	1.37	1.06	1.32	1.44	0.888	1.33
$\langle\epsilon\rangle$ (m^2 s^{-3})	3.9	3.6	3.9	4.0	3.1	4.1	4.3	2.5	4.2
τ_k (ms)	2.0	2.1	2.0	1.9	2.2	1.9	1.9	2.4	1.9
η_k (mm)	0.17	0.18	0.17	0.17	0.18	0.17	0.17	0.19	0.17
$\left\langle \dfrac{\overline{u_1'u_2'}}{u_{1,rms}u_{2,rms}} \right\rangle$	0.0760	0.0880	0.102	0.0988	0.0987	0.796	0.0501	0.105	0.0910

TABLE 1. Turbulence statistics for the higher-energy case ($q^2_{\phi=0} = 1.4\,\mathrm{m^2\,s^{-2}}$).

	B1a	G1at	A1a	B2b	G2bt	A2b	B3a	G3at	A3a
ϕ	0	0.015	0	0	0.099	0	0	0.29	0
$\langle\overline{u}_1\rangle$ (m s^{-1})	0.0940	0.0947	0.0862	0.0552	0.103	0.0772	0.0859	0.107	0.122
$\langle\overline{u}_2\rangle$ (m s^{-1})	0.121	0.121	0.115	0.0262	−0.0916	−0.0703	0.0669	−0.120	0.0199
$\langle u_{1,rms}\rangle$ (m s^{-1})	0.612	0.582	0.589	0.628	0.526	0.613	0.619	0.478	0.602
$\langle u_{2,rms}\rangle$ (m s^{-1})	0.586	0.565	0.572	0.620	0.533	0.601	0.601	0.501	0.585
$\langle q^2\rangle$ (m^2 s^{-2})	1.08	0.989	1.01	1.17	0.842	1.11	1.12	0.722	1.06
$\langle\epsilon\rangle$ (m^2 s^{-3})	2.7	2.5	2.5	3.0	2.2	3.1	2.5	1.3	2.4
τ_k (ms)	2.4	2.5	2.5	2.2	2.6	2.2	2.5	3.4	2.5
η_k (mm)	0.19	0.19	0.19	0.18	0.20	0.18	0.19	0.23	0.19
$\left\langle \dfrac{\overline{u_1'u_2'}}{u_{1,rms}u_{2,rms}} \right\rangle$	0.143	0.132	0.157	0.153	0.117	0.133	0.160	0.130	0.197

TABLE 2. Turbulence statistics for the lower-energy case ($q^2_{\phi=0} = 1.1\,\mathrm{m^2\,s^{-2}}$).

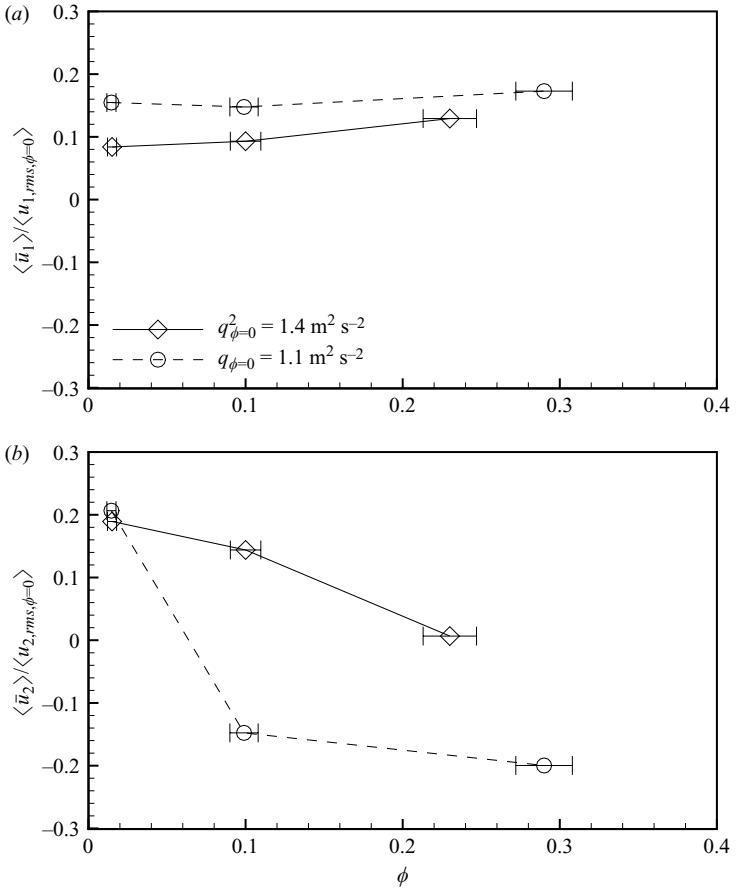

FIGURE 12. Variation of (*a*) horizontal and (*b*) vertical mean velocity with addition of particles.

3.1.1. *Mean flow*

The mean velocity was normalized by the corresponding r.m.s. velocity and is shown in figure 12. The uncertainty for the mean velocity was very small, and thus error bars (which were shorter than the symbol sizes) were not included in the figure. The horizontal mean velocity remained relatively small, of the order of 10–20 % of the unladen horizontal r.m.s. velocity for all cases, as shown in figure 12(*a*). The vertical mean velocity in figure 12(*b*) suggested that the flow at the centre of the chamber was initially directed upwards towards the open particle chute. This can also be confirmed by the pre-unladen mean flow map in figure 4. The upward mean velocity was reduced in magnitude as particles fell through the flow, because the particles dragged air along with them. This can be observed in the mean velocity map of figure 13 for the higher-energy case. The less energetic case had a greater reduction in the vertical mean velocity at similar mass loadings and the mean flow eventually changed direction and became downward with increasing ϕ for this case. Figure 14 shows that the vertical mean velocity was not able to recover fully to its original state, as the secondary flow was influenced by the effective change in the geometry of the chamber owing to the large number of particles that had accumulated on the chamber floor. The mean velocity gradients in the present flow are very small. In

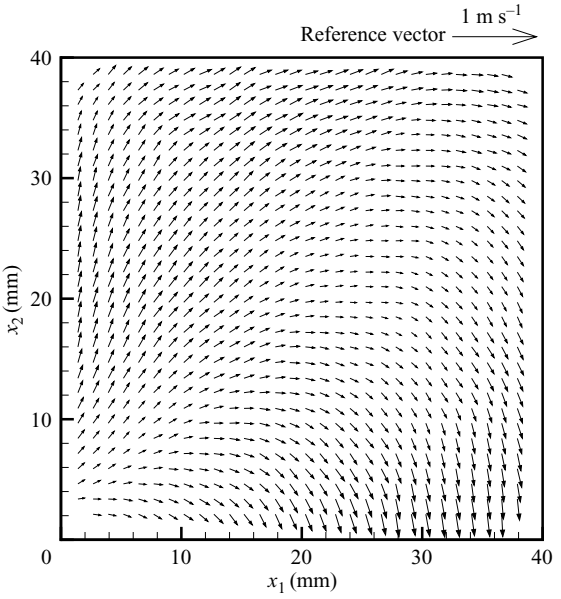

FIGURE 13. Mean fluid velocity field of the particle-laden flow at the highest loading ($\phi = 0.23$) for the higher-energy ($q^2_{\phi=0} = 1.4\,\mathrm{m^2\,s^{-2}}$) case. Three-quarters of the vectors have been removed for clarity.

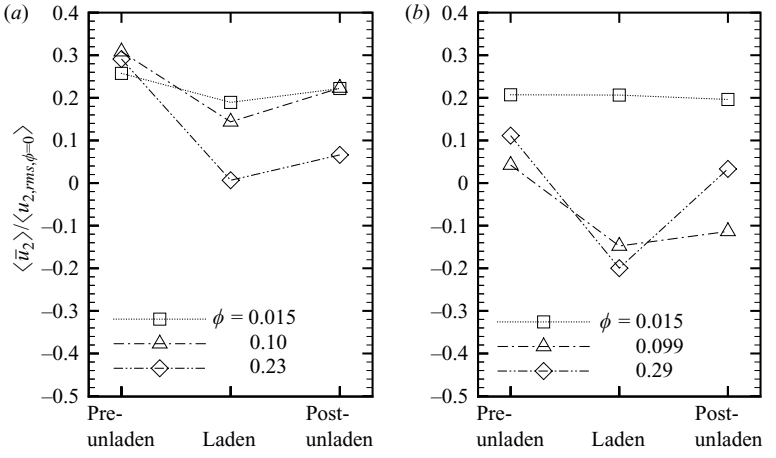

FIGURE 14. Variation of vertical mean velocity with addition of particles for cases (*a*) $q^2_{\phi=0} = 1.4\,\mathrm{m^2\,s^{-2}}$ and (*b*) $q^2_{\phi=0} = 1.1\,\mathrm{m^2\,s^{-2}}$.

typical grid-generated turbulence experiments the turbulence intensity is of the order of 1 % of the mean flow velocity, as opposed to 300–500 % in the present experiment. Therefore, small variations in the mean flow are much less significant in the present experiment than they would be in a wind-tunnel experiment.

3.1.2. *Fluctuating velocities*

The r.m.s. velocities are shown in figure 15. The horizontal r.m.s. velocity showed similar trends for both turbulence levels, as shown in figure 15(*a*). It decreased with increasing mass loading of particles, to less than 80 % of the original value for the

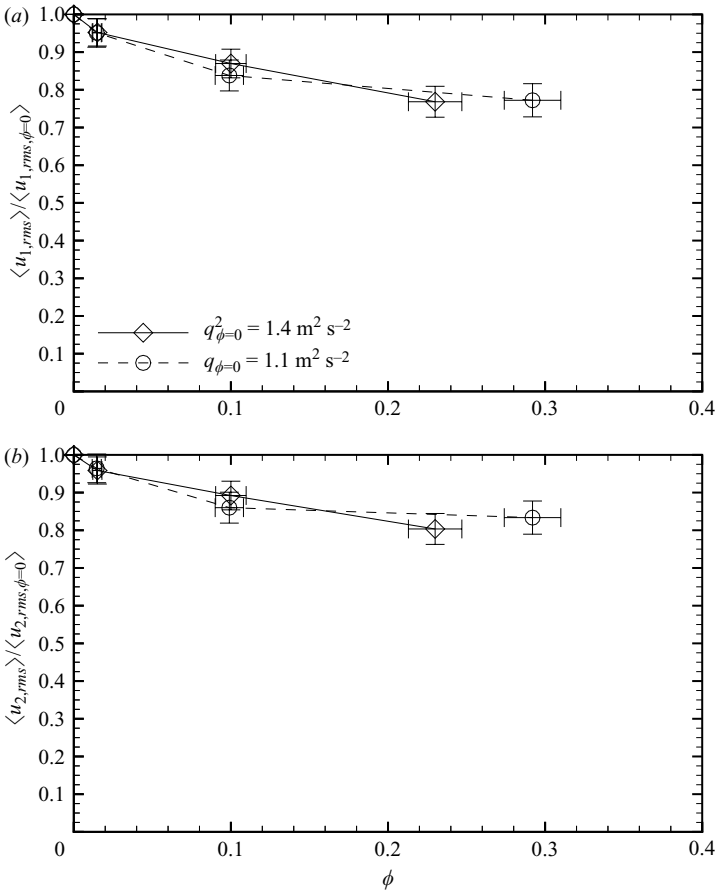

FIGURE 15. Attenuation of (*a*) horizontal and (*b*) vertical r.m.s. velocity with addition of particles.

highest mass loading case. The vertical r.m.s. velocity (figure 15*b*) showed similar trends to the horizontal component. The fluctuating velocities still had Gaussian distributions, as can be seen in figure 16 for the higher-energy case.

The fluctuating velocities were attenuated to a similar degree in the channel flow extension region of the backward-facing step flow described by Fessler & Eaton (1999). Although the two flows are fundamentally different, several similarities do exist at the centre. Fluid fluctuating velocities were both of the order of $1\ \mathrm{m\,s^{-1}}$. The viscous dissipation rates were both near $4.3\ \mathrm{m^2\,s^{-3}}$ and the Kolmogorov length scales were both 0.17 mm. The turbulence was created at the outer edges (by the synthetic jets for the current experiment and by the wall and shear layer for the backward-facing step flow), diffused inwards, and dissipated at the centre. The particles were also both glass beads with similar sizes (165 μm for the current experiment and 150 μm for the backward-facing step flow), Reynolds numbers and Stokes numbers. However, in the backward-facing step flow, the turbulence levels were not modified in the separated shear layer and recovery region, where a substantial number of particles existed. Fessler & Eaton (1999) attributed this to the relative magnitude of the viscous dissipation rate in the different regions, and the lack of residence time of the particles in the flow.

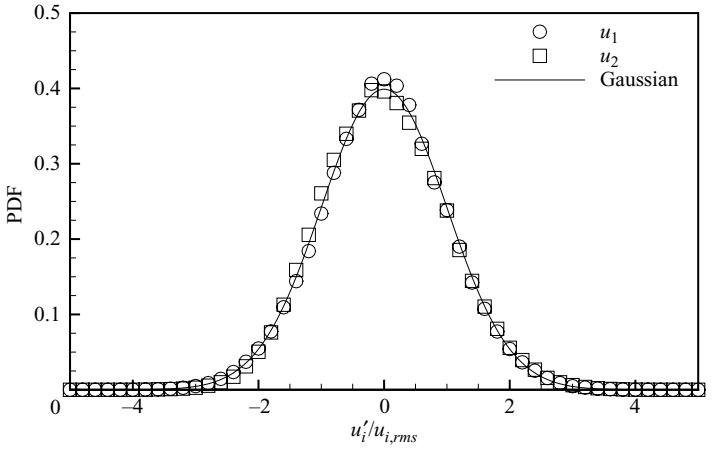

FIGURE 16. Fluctuating fluid velocity PDFs of the particle-laden flow at the highest loading ($\phi = 0.23$) for the higher-energy ($q^2_{\phi=0} = 1.4\,\mathrm{m^2\,s^{-2}}$) case.

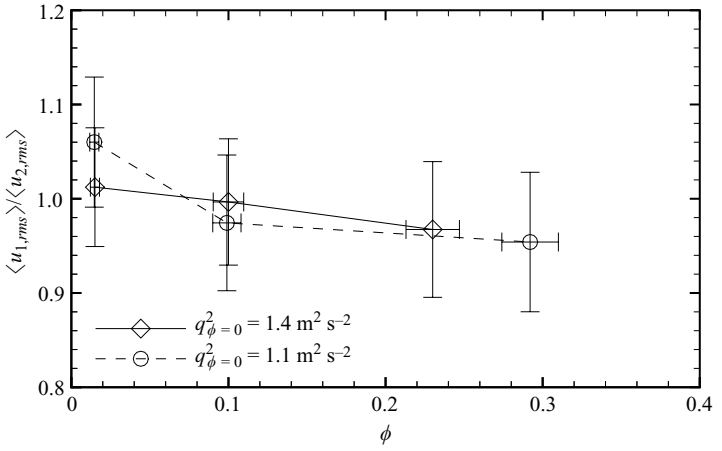

FIGURE 17. Variation of isotropy ratio with addition of particles.

The isotropy ratio was approximately unity, but decreased slightly with the addition of particles for both turbulence levels, as shown in figure 17. This was because the vertical fluctuating velocities were slightly larger than the horizontal fluctuating velocities, owing to the wakes behind individual particles and local jet-like fluid motion caused by clusters of particles that passed through the measurement domain. The isotropy ratio map in figure 18 for the higher-energy case also indicated that the flow was not as isotropic throughout the measurement domain compared to the pre-unladen data set.

3.1.3. *Turbulence kinetic energy and dissipation*

The reduction in r.m.s. velocities corresponded to attenuation of turbulence kinetic energy. Figure 19 shows that q^2 decreased monotonically with increasing particle mass loading for both turbulence levels. Attenuation levels reached almost 40 % for the highest mass loadings of $\phi = 0.23$ ($q^2_{\phi=0} = 1.4\,\mathrm{m^2\,s^{-2}}$ case) and 0.29 ($q^2_{\phi=0} = 1.1\,\mathrm{m^2\,s^{-2}}$ case). The amount of attenuation was significantly greater than that of

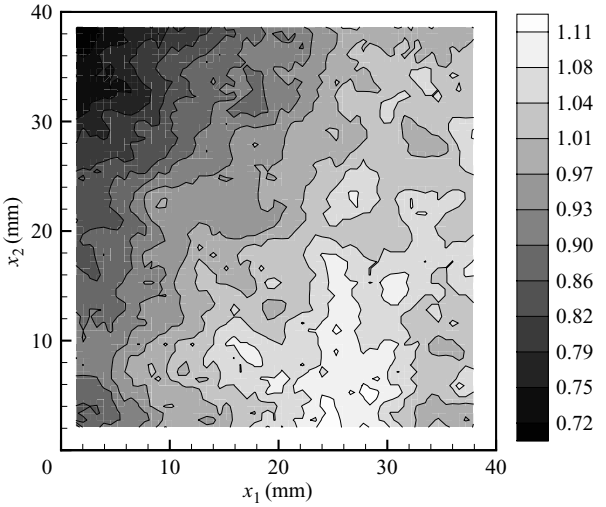

FIGURE 18. Map of isotropy ratio ($u_{1,rms}/u_{2,rms}$) of the particle-laden flow at the highest loading ($\phi = 0.23$) for the higher-energy ($q^2_{\phi=0} = 1.4\,\mathrm{m^2\,s^{-2}}$) case.

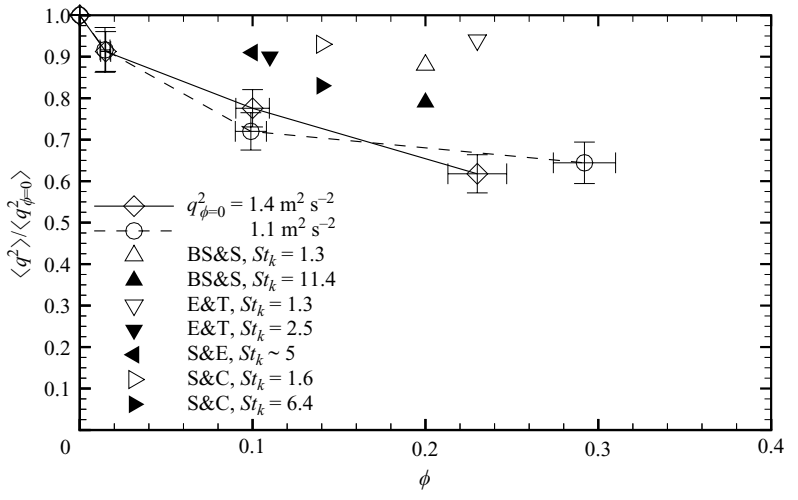

FIGURE 19. Attenuation of turbulence kinetic energy with addition of particles.

the DNS studies of particle-laden homogeneous and isotropic turbulence in table 3, as shown in figure 19. We should note that computational restrictions of DNS make it difficult to simulate realistic experimental conditions of interest, hence the experimental conditions of the data points in figure 19 are all different. Some were conducted in decaying turbulence, the gravity levels were zero, and Re_λ, d_p/η_k, ρ_p/ρ_f, and St_k were all small compared to the present experimental study. Thus, direct comparison between different studies was difficult. Nevertheless, the results indicate that the numerical simulations have not been able to obtain the amount of attenuation observed in the experiments. This suggests that the particle point-force coupling scheme used in most simulations might not be capturing all of the physics. The spatial map of q^2 in figure 20 for the higher-energy case indicated that the turbulence was still fairly homogeneous.

Study	Flow	Re_λ	Re_p	d_p/η_k	ρ_p/ρ_f	St_k	ϕ	α_p ($\times 10^{-4}$)	g (m s^{-2})	$q^2/q^2_{\phi=0}$	$\epsilon/\epsilon_{\phi=0}$
Hwang & Eaton	Stationary turbulence	240	7	0.96	2080	58	0.015	0.072	9.8	0.91	0.91
	($q^2_{\phi=0} = 1.4\,\mathrm{m^2\,s^{-2}}$)	230	7	0.96	2080	59	0.10	0.48	9.8	0.78	0.76
		230	8	0.97	2080	61	0.23	1.1	9.8	0.61	0.59
Boivin *et al.* (1998)	Stationary turbulence	62	0.38	0.11		1.3	0.2		0	0.88	0.65
		62	1.52	0.35		11.4	0.2		0	0.79	0.53
Elghobashi & Truesdell (1993)	Decaying turbulence	35	0.18	0.16	909	1.3	0.23	2.5	0	0.94	1.05
		35	0.45	0.32	455	2.5	0.11	2.5	0	0.90	
Squires & Eaton (1990)	Stationary turbulence	38	$\ll 1$	< 1	$\gg 1$	~ 5	0.1		0	0.91	0.86
Sundaram & Collins (1999)	Decaying turbulence	94		0.18	900	1.6	0.14	1.8	0	0.93	1.21
		94		0.36	900	6.4	0.14	1.8	0	0.83	1.15

TABLE 3. Parameters for homogeneous and isotropic turbulence studies, all of which are DNS except the present study. Initial and unladen values are used for the basis of comparison, except for the change in the turbulence kinetic energy and ϵ, which use final values at the end of the simulations.

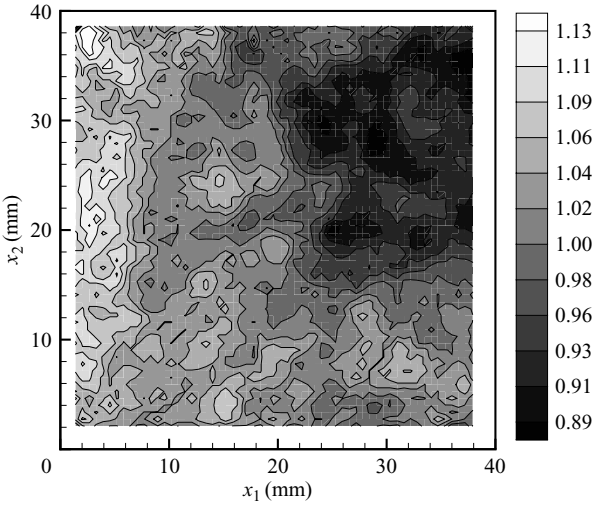

FIGURE 20. Map of the turbulence kinetic energy normalized by the spatial average ($q^2/\langle q^2\rangle$) of the particle-laden flow at the highest loading ($\phi = 0.23$) for the higher-energy case ($q^2_{\phi=0} = 1.4\,\mathrm{m^2\,s^{-2}}$).

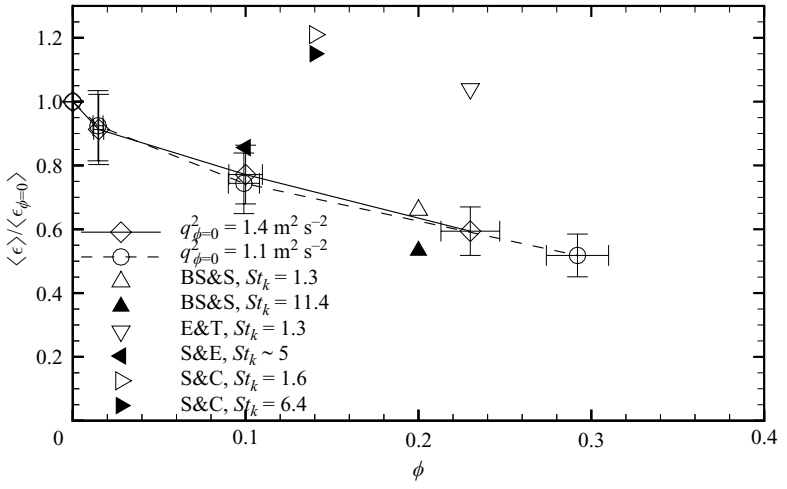

FIGURE 21. Attenuation of viscous dissipation rate with addition of particles.

The attenuation of ϵ with particle mass loading is shown in figure 21. Attenuation levels were similar for both turbulence levels, and reached 40–50 % for the highest mass loadings. This was slightly greater than the attenuation levels of the turbulence kinetic energy. There is some question whether the dynamic equilibrium assumption for calculating ϵ is fully valid for this experiment when particles are present. Thus, the absolute magnitude of the dissipation rate quoted may not be exact. Nevertheless, we believe that the method does properly capture the relative changes in the dissipation rate between cases. The term ϵ was attenuated similarly for the stationary turbulence studies of Squires & Eaton (1990) and Boivin *et al.* (1998), while it was slightly augmented for the decaying turbulence studies of Elghobashi & Truesdell (1993) and Sundaram & Collins (1999). The decrease in ϵ resulted in an increase of the Kolmogorov time and length scales.

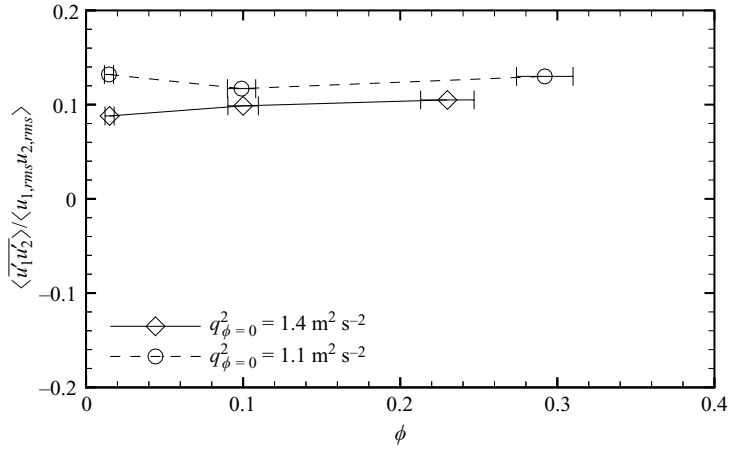

FIGURE 22. Variation of Reynolds shear stress with addition of particles.

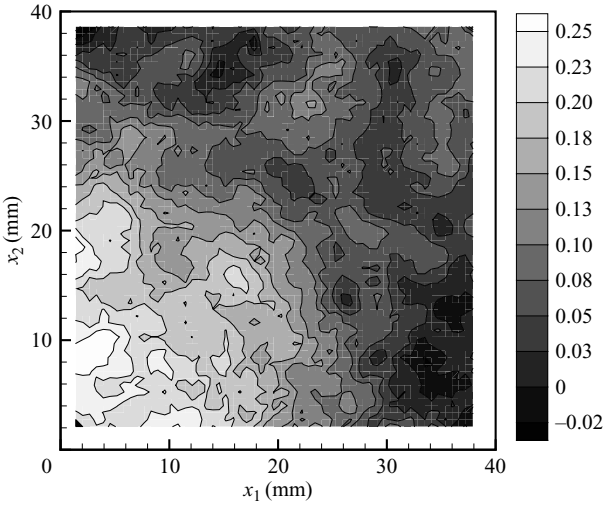

FIGURE 23. Shear-stress correlation coefficient map for the particle-laden flow at the highest loading ($\phi = 0.23$) for the higher-energy ($q^2_{\phi=0} = 1.4\,\mathrm{m^2\,s^{-2}}$) case.

3.1.4. *Reynolds shear stress*

The Reynolds shear stress had non-zero values for the particle-laden flow experiments, although in all cases it remained small. Figure 22 shows that the shear-stress correlation coefficient was positively biased at 0.1 for the higher-energy case, and slightly higher for the lower-energy case owing to the relatively stronger effect of the mean flow. The shear-stress correlation coefficient was not correlated with the particle mass loading, as it had similar values for increasing ϕ. The positive bias in the shear-stress correlation coefficient could also be observed in the spatial map in figure 23 for the higher-energy case. The PDF in figure 24 indicates that the primary peak coincides with that of the pre-unladen case in figure 7, and is thus probably due to the effects of the particle chute connected to the top of the chamber. The secondary peak at around 0.18 is probably due to mean shear in the flow caused by the settling particles.

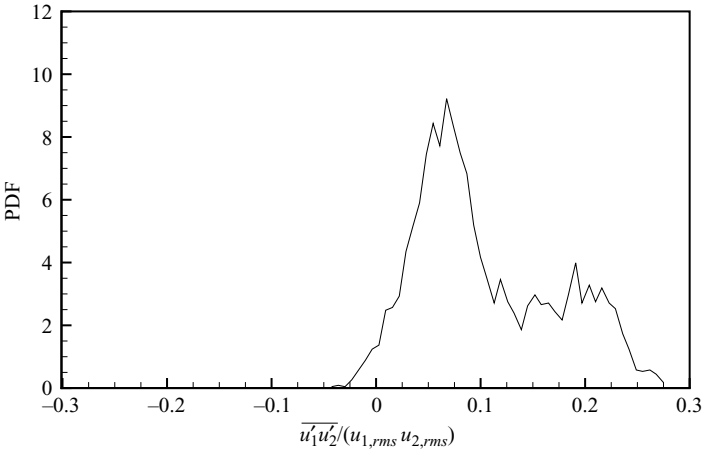

FIGURE 24. Shear-stress correlation coefficient PDF for the particle-laden flow at the highest loading ($\phi = 0.23$) for the higher-energy ($q^2_{\phi=0} = 1.4\,\mathrm{m^2\,s^{-2}}$) case.

3.2. *Two-point spatial velocity correlations*

Two-point spatial velocity correlations for the pre-unladen data sets corresponding to different ϕ coincided well for each correlation, indicating that the results were repeatable. Longitudinal correlations were plotted for different ϕ and compared to the average correlation coefficient of the pre-unladen data sets in figure 25 for the higher-energy case. The separation distance was normalized by the average Kolmogorov length scale of the three pre-unladen data sets. As increasing numbers of particles were dropped through the flow, the longitudinal correlation of the horizontal fluctuating velocities in figure 25(*a*) did not deviate from the average pre-unladen curve. That is, there was no significant distortion of the turbulence structure evident in this correlation by particles. On the other hand, the longitudinal correlation increased at large separation distances and decreased at small separation distances (as shown in the close-up in the insert) for the vertical fluctuating velocities (figure 25*b*). Although individual velocity vectors had uncertainties, the averaged product of two vectors at small separation distances had very small uncertainties because the number of samples was very large (e.g. 3.4 million over 1000 image pairs for the smallest separation distance). The increase at large separation distances could possibly have been due to particle clusters transferring energy to the flow via local jet-like fluid motion as they settled. The consistent trend of decrease at small separation distances (which again demonstrates the small overall uncertainty in this region) corresponded to a decrease in the Taylor microscale and suggested that individual particles extracted energy through small-scale extra dissipation near the particle surface (described in detail in § 3.4). Similar trends were observed for the lower-energy case.

3.3. *Energy spectra*

The energy spectrum measurement was limited to an intermediate wavenumber range, and thus we could not fully resolve the integral or Kolmogorov length scales. Nonetheless, the spectra provide some useful insights. It should be noted that we are only making limited observations of the changes in spectral content of the energy,

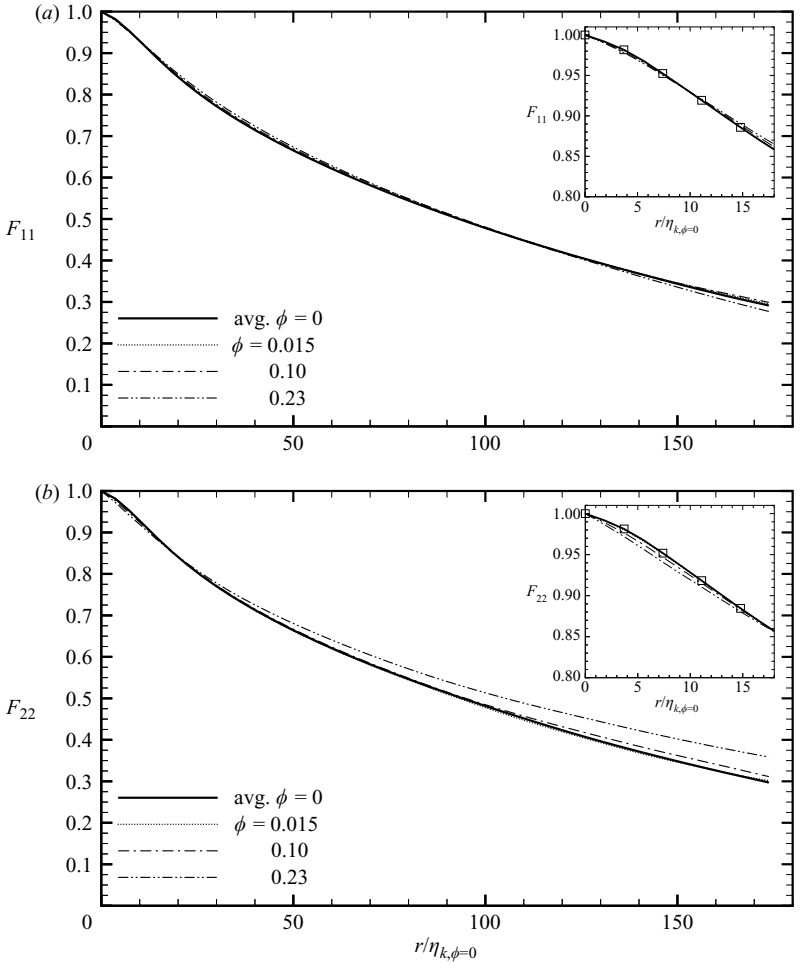

FIGURE 25. Two-point longitudinal velocity correlations of the particle-laden flow for the higher-energy ($q^2_{\phi=0} = 1.4\,\mathrm{m^2\,s^{-2}}$) case in the (*a*) horizontal and (*b*) vertical directions.

not the overall energy. The overall turbulence kinetic energy attenuation is obtained from the turbulence kinetic energy measurements, not the energy spectra.

The radial energy spectra for the particle-laden flow are shown in figure 26 for the higher-energy case. The wavenumber was normalized by the average pre-unladen Kolmogorov length scale, and the average pre-unladen spectrum is shown for comparison. Increasing the mass loading of particles increasingly attenuated the horizontal component of the spectrum in the measurable wavenumber range (figure 26*a*). The attenuation was fairly uniform across all measurable wavenumbers. The attenuation for the vertical component was fairly uniform at lower wavenumbers (figure 26*b*), but decreased at higher wavenumbers. This suggests that spectral cross-over might have occurred at higher wavenumbers beyond those resolved here (see e.g. Squires & Eaton 1990; Boivin *et al.* 1998; Sundaram & Collins 1999). The vertical component also had larger energy than the horizontal component, indicating that the flow was not as isotropic as before. This was probably due to the vertical flow disturbances caused by the particles.

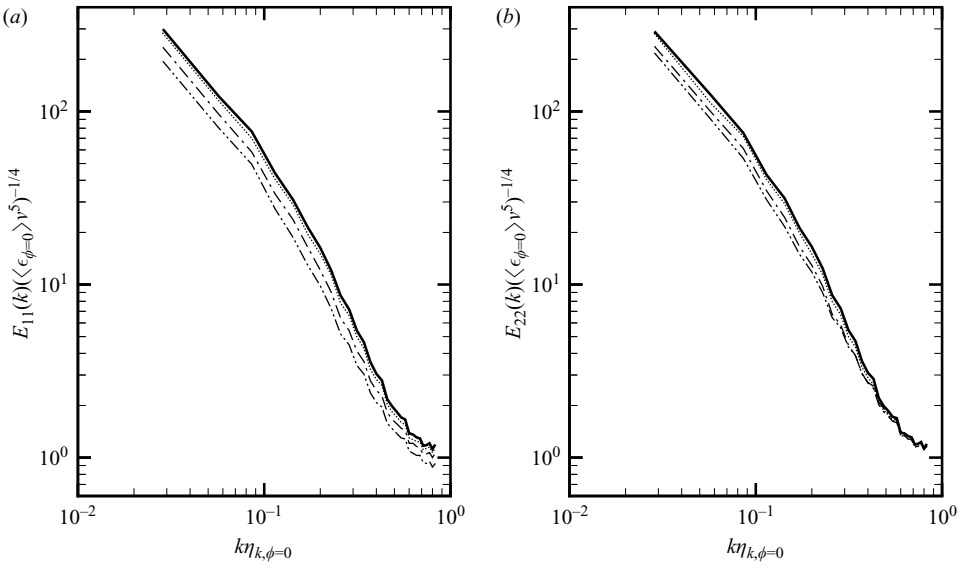

FIGURE 26. Radial energy spectra of the particle-laden flow for the higher-energy case ($q^2_{\phi=0}=1.4\,\mathrm{m^2\,s^{-2}}$) for the (*a*) horizontal and (*b*) vertical velocity components: —, avg. $\phi = 0$; ···, $\phi = 0.015$; — · —, $\phi = 0.10$; — ·· —, $\phi = 0.23$.

3.4. *Energy budget*

To help understand the coupling between the particles and turbulence, an energy budget analysis of the turbulent flow was conducted, taking the $40 \times 40 \times 0.5\,\mathrm{mm}^3$ measurement domain as the control volume. Assuming an overall steady-state process for the fluid in the control volume, the energy budget for the fluid-phase kinetic energy could be written as

$$\dot{E}_i - \dot{E}_o + \dot{E}_p - \dot{E}_s = 0, \tag{3.1}$$

where $\dot{E}_i$ and $\dot{E}_o$ represent rates of energy input and output, respectively, and $\dot{E}_p$ and $\dot{E}_s$ represent rates of energy production and sink, respectively. $\dot{E}_i - \dot{E}_o$ could be considered a net energy input into the control volume by transport and diffusion of turbulence kinetic energy from the synthetic jet actuators. This was possible because the turbulence was not perfectly homogeneous. Each particle lost potential energy as it fell through the flow. Since the particles fell at a certain settling velocity, the lost gravitational potential energy was an input of energy into the fluid in the control volume. This energy appeared as wakes of individual particles and as local jets produced by falling particle clusters. Some of the energy was dissipated directly by viscous effects near the particle surface at scales significantly smaller than the smallest turbulent eddies. In the accounting below, this viscous dissipation is bundled into the 'extra dissipation due to particles' term. It should be noted that this type of analysis is universal in nature. For instance, it can be performed for the backward-facing step flow of Fessler & Eaton (1999) mentioned in § 3.1.2, with the net energy input being the transport of energy from the wall boundary layer and the separated shear layer, and the other terms being the same.

Equation (3.1) can now be written as

$$\dot{E}_{i,sja} + \phi g v_t - \dot{E}_s = 0, \tag{3.2}$$

where $\dot{E}_{i,sja}$ is the input from the synthetic jet actuators, g is acceleration due to gravity, and v_t is the settling velocity of particles in the turbulence. The only energy sink is viscous dissipation that we choose to split, for the sake of discussion into two components, the ordinary viscous dissipation of turbulence energy and the extra dissipation due to particles. The normal viscous dissipation in single-phase flow is a result of the turbulence cascade from large-scale energy-containing eddies to smaller dissipating scales. The extra dissipation due to particles is the viscous dissipation due to small-scale motions in the vicinity of particles, and can also be described as 'unresolved dissipation'. Particles moving at a velocity different from the surrounding flow produce very small-scale local disturbances that are dissipated by viscosity. In one sense, both the ordinary viscous dissipation of the turbulence kinetic energy and the extra dissipation due to particles are different manifestations of the same physical mechanism. However, the extra dissipation occurs mostly at scales smaller than those produced by the turbulence cascade, and was not resolved in our measurements. In that sense, these two dissipation rates may be thought of as separate energy sinks.

Large-scale flow distortions might also have been produced by individual particles and particle clusters as they fell through the flow. There are two ways to view the effects of these flow distortions. The first approach is to assume that the flow distortions are at the same length scale as the regular turbulence and indistinguishable from it, considering that the average inter-particle spacing was approximately $15\eta_k$. The dissipation for these flow distortions would be accounted for in the measurements of the viscous dissipation. That means the extra dissipation due to particles would appear as the only energy sink caused by the particles. Equation (3.2) could then be written as

$$\dot{E}_{i,sja} + \phi g v_t - \epsilon - \epsilon_p = 0, \tag{3.3}$$

where ϵ is the resolved dissipation rate and ϵ_p is the extra dissipation rate due to particles.

The value of each term in (3.3) was estimated from the consecutive pre-unladen and laden data sets for the higher-energy case corresponding to the highest mass loading of $\phi = 0.23$. It was difficult to measure directly the energy input rate from the speakers, so it was indirectly estimated from the viscous dissipation rate in the pre-unladen data set, assuming that the energy transported from the synthetic jet actuators was all dissipated:

$$\dot{E}_{i,sja} = \epsilon_{\phi=0}. \tag{3.4}$$

This value was $4.3\,\mathrm{m^2\,s^{-3}}$. The production in the fluid due to the loss of potential energy of the particles was $1.3\,\mathrm{m^2\,s^{-3}}$ for $\phi = 0.23$ and $v_t = 0.59\,\mathrm{m\,s^{-1}}$, which was obtained in a separate experiment by measuring the velocities of particles (using PTV) falling through turbulent flow that was not seeded. The viscous dissipation rate for the particle-laden data set was measured to be $2.5\,\mathrm{m^2\,s^{-3}}$. The extra dissipation due to particles could thus be obtained by difference as approximately $3.1\,\mathrm{m^2\,s^{-3}}$.

This extra dissipation might seem larger than one might expect. The standard model that has been used to estimate this extra dissipation (Elghobashi & Abou-Arab 1983; Rogers & Eaton 1991) assumes a quasi-steady particle drag law using a nonlinear correction to the standard Stokes drag. It is written as

$$\epsilon_p = \frac{\overline{c}}{\rho_f \tau_{p,s}}(\overline{u_i' u_i'} - \overline{u_i' v_i'}) + \frac{1}{\rho_f \tau_{p,s}}(\overline{c' u_i' u_i'} - \overline{c' u_i' v_i'}) + \frac{1}{\rho_f \tau_{p,s}}(\overline{u}_i - \overline{v}_i)\overline{c' u_i'}, \tag{3.5}$$

where $\overline{c}$ and c' denote the mean and fluctuating particle concentrations, and $\overline{v}$ and v' denote the mean and fluctuating particle velocities. For unresponsive, large St_k particles, the particle distribution is uncorrelated to the fluid velocity field and the fluid–particle fluctuating velocity correlation is small. The extra dissipation from this model can thus be reduced to

$$\epsilon_p \simeq \frac{\overline{c}}{\rho_f \tau_{p,s}} (\overline{u_i' u_i'}), \tag{3.6}$$

which was estimated to be $0.32\,\mathrm{m^2\,s^{-3}}$, nearly an order of magnitude smaller than the estimated value of $3.1\,\mathrm{m^2\,s^{-3}}$ from (3.3). However, (3.6) often underpredicts ϵ_p. The assumptions employed to obtain (3.5) are essentially the same as those used to develop point-force coupled simulation codes. Segura, Eaton & Oefelein (2004) showed evidence that such codes underpredict ϵ_p by about an order of magnitude. Studies such as those of Squires & Eaton (1990), Elghobashi & Truesdell (1993), Boivin *et al.* (1998), and Sundaram & Collins (1999) in figure 19 used highly accurate DNS of the fluid flow coupled with such oversimplified descriptions of the particle dynamics, and were not able to obtain the same amount of attenuation observed in the experiments, possibly due to this underprediction of the extra dissipation by particles. One reason for this underprediction might be the inadequate assumption of quasi-steady drag when the particle near field is highly unsteady. Several recent studies by Coimbra, Rangel and co-workers have pointed out that the Basset drag force, which is neglected in the 'standard model' of (3.5), can have a significant effect on the total drag (Coimbra & Rangel 2001; Coimbra *et al.* 2004; L'Esperance *et al.* 2005).

Fessler & Eaton (1999) also noted that (3.6) does not fully capture the effects of the particles on the flow. It contradicts experimental results because it is inversely proportional to the particle time constant and thus the Stokes number. It also does not take into account the different turbulence modification in different flow regimes they had observed in their backward-facing step flow. They suggested that the particles change the flow structure, and inherently the fluid dissipation, which has indirect effects on the turbulence kinetic energy equation. If they had measured the viscous dissipation in the laden flow, they could also have estimated the ϵ_p from an equation similar to (3.3) and compared with (3.6).

The second approach assumes that the particles distort the flow in such a way that the large energetic eddies are greatly disturbed. This idea may seem feasible if we consider the particles as a series of screens with an average mesh spacing of $15\eta_k$ continuously falling through the turbulence. Eaton *et al.* (1999) demonstrated that the flow distortions due to particles with $Re_p \sim 10$ extend several particle diameters (or η_k in our case, since $d_p \sim \eta_k$) downstream. Not only do the particles add turbulence to the flow through particle wakes, but the energetic flow structure can be destroyed by this 'screen effect'. Considering that particle clusters 10–20 mm wide sometimes fell through the turbulent flow which had an integral length scale of approximately 80 mm, this seems even more plausible. This destruction in flow structure would have to be accounted for as a sink separate from ϵ_p, as the viscous dissipation that is measured only takes into account the turbulent energy that is being cascaded down to smaller scales from the disturbed flow. $\dot{E}_s$ would thus be written as

$$\dot{E}_s = \epsilon + \epsilon_p + \dot{E}_{s,se}, \tag{3.7}$$

where $\dot{E}_{s,se}$ is the energy sink due to this 'screen effect'. It is not clear how large this term would be compared to ϵ_p, but the sum $\epsilon_p + \dot{E}_{s,se}$ should be $3.1\,\mathrm{m^2\,s^{-3}}$ from (3.3).

It is unclear as to which approach describes the large-scale flow distortions more accurately. The energy sink due to particles is possibly a combination of both effects.

4. Summary

A dilute dispersion of small dense particles with diameters of the order of the Kolmogorov length scale and Stokes numbers near 50 were found experimentally to cause significant attenuation of homogeneous isotropic turbulence at mass loadings of 0.3 and less. At the highest mass loadings, the turbulent kinetic energy was reduced by approximately 40 %. This degree of attenuation was significantly greater than that predicted by point-force coupled DNS models indicating that improved force-coupling models are required.

The particles falling under the influence of gravity affected the isotropy of the flow. The radial energy spectra showed increasing attenuation of the horizontal component with increasing mass loading. The attenuation was uniform across all measurable wavenumbers. Conversely, the vertical component showed a similar level of attenuation at low wavenumbers, but the amount of attenuation decreased at higher wavenumbers. This was a clear indication that the falling particles added energy at high wavenumbers.

The turbulent kinetic energy viscous dissipation rate was measured using an approximate technique which did not resolve small-scale dissipation owing to local distortions around the particles. The resolved dissipation rate decreased by 40–50 % at the heaviest particle loading. An energy budget for the gas-phase turbulence at the centre of the test chamber showed that the unresolved turbulent kinetic energy dissipation rate was comparable to the regular resolved dissipation. This indicates that local distortion of turbulence around particles plays a very significant role in the overall attenuation of turbulence.

We would like to acknowledge the support of the National Aeronautics and Space Administration, which sponsored this research through grant numbers NCC3-640 and NAG3-2738 under the supervision of Dr Nasser Rashidnia. We are also grateful for the help of Eon-Soo Lee in conducting the experiments.

REFERENCES

Boivin, M., Simonin, O. & Squires, K. D. 1998 Direct numerical simulation of turbulence modulation by particles in isotropic turbulence. *J. Fluid Mech.* **375**, 235–263.

Boivin, M., Simonin, O. & Squires, K. D. 2000 On the prediction of gas–solid flows with two-way coupling using large eddy simulation. *Phys. Fluids* **12**, 2080–2090.

Bracewell, R. N. 1995 *Two-Dimensional Imaging*. Prentice–Hall.

Burton, T. M. & Eaton, J. K. 2003 Fully resolved simulations of particle–turbulence interaction. *Tech. Rep.* TSD-151. Stanford University.

Carlson, C. R. & Peskin, R. L. 1975 One-dimensional particle probability densities measured in turbulent gas–particle duct flow. *Intl J. Multiphase Flow* **2**, 67–78.

Chen, J.-H., Wu, J.-S. & Faeth, G. M. 2000 Turbulence generation in homogeneous particle-laden flows. *AIAA J.* **38**, 636–642.

Coimbra, C. F. M. & Rangel, R. H. 2001 Spherical particle motion in harmonic Stokes flows. *AIAA J.* **39**, 1673–1682.

Coimbra, C. F. M., L'Esperance, D., Lambert, R. A., Trolinger, J. D. & Rangel, R. H. 2004 An experimental study on stationary history effects in high-frequency Stokes flows. *J. Fluid Mech.* **504**, 353–363.

Druzhinin, O. A. 2001 The influence of particle inertia on the two-way coupling and modification of isotropic turbulence by microparticles. *Phys. Fluids* **13**, 3738–3755.

Druzhinin, O. A. & Elghobashi, S. 1999 On the decay rate of isotropic turbulence laden with microparticles. *Phys. Fluids* **11**, 602–610.

Eaton, J. K. 1994 Experiments and simulations on turbulence modification by dispersed particles. *Appl. Mech. Rev.* **47**, 544–548.

Eaton, J. K., Paris, A. D. & Burton, T. M. 1999 Local distortion of turbulence by dispersed particles. *AIAA Paper* 99-3643.

Elghobashi, S. 1994 On predicting particle-laden turbulent flows. *Appl. Sci. Res.* **52**, 309–329.

Elghobashi, S. & Truesdell, G. C. 1993 On the two-way interaction between homogeneous turbulence and dispersed solid particles. I: Turbulence Modification. *Phys. Fluids* A **5**, 1790–1801.

Elghobashi, S. E. & Abou-Arab, T. W. 1983 A two-equation turbulence model for two-phase flows. *Phys. Fluids* **26**, 931–938.

Ferrante, A. & Elghobashi, S. 2003 On the physical mechanisms of two-way coupling in particle-laden isotropic turbulence. *Phys. Fluids* **15**, 315–329.

Fessler, J. R. & Eaton, J. K. 1999 Turbulence modification by particles in a backward-facing step flow. *J. Fluid Mech.* **394**, 97–117.

Geiss, S., Dreizler, A., Stojanovic, Z., Chrigui, M., Sadiki, A. & Janicka, J. 2004 Investigation of turbulence modification in a non-reactive two-phase flow. *Exps. Fluids* **36**, 344–354.

Gonzalez, R. C. & Woods, R. E. 1993 *Digital Image Processing*. Addison–Wesley.

Gore, R. A. & Crowe, C. T. 1989 Effect of particle size on modulating turbulence intensity. *Intl J. Multiphase Flow* **15**, 279–285.

Gotoh, T., Fukayama, D. & Nakano, T. 2002 Velocity statistics in homogeneous steady turbulence obtained using a high-resolution direct numerical simulation. *Phys. Fluids* **14**, 1065–1081.

Han, D. 2001 Study of turbulent nonpremixed jet flames using simultaneous measurements of velocity and CH distribution. *Tech. Rep.* TSD-134. Stanford University.

Hardalupas, Y., Taylor, A. M. K. P. & Whitelaw, J. H. 1992 Particle dispersion in a vertical round sudden expansion flow. *Proc. R. Soc. Lond.* A **341**, 411–442.

Hasselbrink, E. F. & Mungal, M. G. 2001 Transverse jets and jet flames. Part 2. Velocity and OH field imaging. *J. Fluid Mech.* **443**, 27–68.

Hetsroni, G. 1989 Particles–turbulence interaction. *Intl J. Multiphase Flow* **15**, 735–746.

Hishida, K. & Maeda, M. 1991 Turbulence characteristics of particle-laden flow behind a rearward facing step. *ASME FED* **121**, 207–212.

Hwang, W. & Eaton, J. K. 2004*a* Creating homogeneous and isotropic turbulence without a mean flow. *Exps. Fluids* **36**, 444–454.

Hwang, W. & Eaton, J. K. 2004*b* Modification of homogeneous and isotropic turbulence by solid particles. *Tech. Rep.* TF-89. Stanford University.

Kiger, K. T. & Pan, C. 2000 PIV technique for the simultaneous measurement of dilute two-phase flows. *Trans. ASME* I: *J. Fluids Engng* **122**, 811–818.

Kiger, K. T. & Pan, C. 2002 Suspension and turbulence modification effects of solid particulates on a horizontal turbulent channel flow. *J. Turb.* **3**, 1–21.

Kulick, J. D., Fessler, J. R. & Eaton, J. K. 1994 Particle response and turbulence modification in fully developed channel flow. *J. Fluid Mech.* **277**, 109–134.

Kussin, J. & Sommerfeld, M. 2002 Experimental studies on particle behaviour and turbulence modification in horizontal channel flow with different wall roughness. *Exps. Fluids* **33**, 143–159.

Lee, S. L. & Durst, F. 1982 On the motion of particles in turbulent duct flows. *Intl J. Multiphase Flow* **8**, 125–146.

L'Esperance, D., Coimbra, C. F. M., Trolinger, J. D. & Rangel, R. H. 2005 Experimental verification of fractional history effects on the viscous dynamics of small spherical particles. *Exps. Fluids* **38**, 112–116.

Liu, S., Meneveau, C. & Katz, J. 1994 On the properties of similarity subgrid-scale models as deduced from measurements in a turbulent jet. *J. Fluid Mech.* **275**, 83–119.

Liu, S., Katz, J. & Meneveau, C. 1999 Evolution and modelling of subgrid scales during rapid straining of turbulence. *J. Fluid Mech.* **387**, 281–320.

Maeda, M., Hishida, K. & Furutani, T. 1980 Optical measurements of local gas and particle velocity in an upward flowing dilute gas–solids suspension. In *Polyphase Flow and Transport Technology, Century 2-ETC, San Francisco*, pp. 211–216.

Maxey, M. R., Patel, B. K., Chang, E. J. & Wang, L.-P. 1997 Simulations of dispersed turbulent multiphase flow. *Fluid Dyn. Res.* **20**, 143–156.

Mizukami, M., Parthasarathy, R. N. & Faeth, G. M. 1992 Particle-generated turbulence in homogeneous dilute dispersed flows. *Intl J. Multiphase Flow* **18**, 397–412.

Nishino, K. & Matsushita, H. 2004 Columnar particle accumulation in homogeneous turbulence. In *Proc. 5th Intl Conf. on Multiphase Flows, Yokohama.*

Paris, A. D. & Eaton, J. K. 2001 Turbulence attenuation in a particle-laden channel flow. *Tech. Rep.* TSD-137. Stanford University.

Parthasarathy, R. N. & Faeth, G. M. 1990 Turbulence modulation in homogeneous dilute particle-laden flows. *J. Fluid Mech.* **220**, 485–514.

Raffel, M., Willert, C. & Kompenhans, J. 1998 *Particle Image Velocimetry: A Practical Guide*. Springer.

Rogers, C. B. & Eaton, J. K. 1991 The effect of small particles on fluid turbulence in a flat-plate, turbulent boundary layer in air. *Phys. Fluids* A **3**, 928–937.

Roth, G. I. & Katz, J. 2001 Five techniques for increasing the speed and accuracy of PIV interrogation. *Meas. Sci. Technol.* **12**, 238–245.

Sato, Y. & Hishida, K. 1996 Transport process of turbulence energy in particle-laden turbulent flow. *Intl J. Heat Fluid Flow* **17**, 202–210.

Sato, Y., Hishida, K., Simonin, O. & Squires, K. 2000 On turbulence modulation by particles. In *Proc. 3rd Intl Symp. Turbulence, Heat, and Mass Transfer, Nagoya,* pp. 939–946.

Schreck, S. & Kleis, S. 1993 Modification of grid-generated turbulence by solid particles. *J. Fluid Mech.* **249**, 665–688.

Segura, J. C., Eaton, J. K. & Oefelein, J. C. 2004 Predictive capabilities of particle-laden large eddy simulation. *Tech. Rep.* TSD-156. Stanford University.

Sheng, J., Meng, H. & Fox, R. O. 2000 A large eddy PIV method for turbulence dissipation rate estimation. *Chem. Engng Sci.* **55**, 4423–4434.

Squires, K. D. & Eaton, J. K. 1990 Particle response and turbulence modification in isotropic turbulence. *Phys. Fluids* A **2**, 1191–1203.

Sundaram, S. & Collins, L. R. 1999 A numerical study on the modulation of isotropic turbulence by suspended particles. *J. Fluid Mech.* **379**, 105–143.

Suzuki, Y., Ikenoya, M. & Kasagi, N. 2000 Simultaneous measurement of fluid and dispersed phases in a particle-laden turbulent channel flow with the aid of 3-D PTV. *Exps. Fluids* **29**, S185–S193.

Tsuji, Y. & Morikawa, Y. 1982 LDV measurements of an air-solid two-phase flow in a horizontal pipe. *J. Fluid Mech.* **120**, 385–409.

Tsuji, Y., Morikawa, Y. & Shiomi, H. H. 1984 LDV measurements of an air-solid two-phase flow in a vertical pipe. *J. Fluid Mech.* **139**, 417–434.

Willert, C. & Gharib, M. 1991 Digital particle image velocimetry. *Exps. Fluids* **10**, 181–193.

Wood, A. M., Hwang, W. & Eaton, J. K. 2005 Preferential concentration of particles in homogeneous and isotropic turbulence. *Intl J. Multiphase Flow* **31**, 1220–1230.

Yang, T. S. & Shy, S. S. 2005 Two-way interaction between solid particles and homogeneous air turbulence: particle settling rate and turbulence modification measurements. *J. Fluid Mech.* **526**, 171–216.

Yeung, P. K. & Zhou, Y. 1997 Universality of the Kolmogorov constant in numerical simulations of turbulence. *Phys. Rev.* E **56**, 1746–1752.